21. M. K. Pető, S. Mukhopadhyay, K. A. Kelley, *Earth Planet. Sci. Lett.* **369–370**, 13–23 (2013).
22. M. G. Jackson, S. B. Shirey, E. H. Hauri, M. D. Kurz, H. Rizo, *Geochim. Cosmochim. Acta* 10.1016/j.gca.2016.02.011 (2016).
23. J. P. Brandenburg, E. H. Hauri, P. E. van Keken, C. J. Ballentine, *Earth Planet. Sci. Lett.* **276**, 1–13 (2008).
24. E. J. Garnero, A. K. McNamara, *Science* **320**, 626–628 (2008).
25. M. Horan, R. J. Walker, J. W. Morgan, J. N. Grossman, A. E. Rubin, *Chem. Geol.* **196**, 27–42 (2003).
26. T. J. Ireland, R. J. Walker, M. O. Garcia, *Chem. Geol.* **260**, 112–128 (2009).
27. W. B. Tonks, H. J. Melosh, *J. Geophys. Res. Planets* **98**, 5319–5333 (1993).

ACKNOWLEDGMENTS

We thank T. Mock for assistance with mass spectrometry. This work was improved by helpful discussions with J. O'Neil, S. Shirey, and B. Wood. We thank S. Shirey, who provided sample VE-32. We also appreciate the helpful comments and suggestions from three anonymous reviewers. We thank M. Garçon, who developed the four-step ^{142}Nd acquisition method. This work was supported by NSF grant EAR-1265169 (Cooperative Studies of the Earth's Deep Interior program) to R.J.W. and grant EAR-1250419 to S.M. All data are available in the main manuscript and supplementary materials.

SUPPLEMENTARY MATERIALS

www.sciencemag.org/content/352/6287/809/suppl/DC1
Materials and Methods
Figs. S1 to S6
Tables S1 to S5
References (*28*–*56*)

12 November 2015; accepted 5 April 2016
10.1126/science.aad8563

SLEEP RESEARCH

Causal evidence for the role of REM sleep theta rhythm in contextual memory consolidation

Richard Boyce,[1] Stephen D. Glasgow,[2] Sylvain Williams,[2]*† Antoine Adamantidis[2,3]*†

Rapid eye movement sleep (REMS) has been linked with spatial and emotional memory consolidation. However, establishing direct causality between neural activity during REMS and memory consolidation has proven difficult because of the transient nature of REMS and significant caveats associated with REMS deprivation techniques. In mice, we optogenetically silenced medial septum γ-aminobutyric acid–releasing (MS^{GABA}) neurons, allowing for temporally precise attenuation of the memory-associated theta rhythm during REMS without disturbing sleeping behavior. REMS-specific optogenetic silencing of MS^{GABA} neurons selectively during a REMS critical window after learning erased subsequent novel object place recognition and impaired fear-conditioned contextual memory. Silencing MS^{GABA} neurons for similar durations outside REMS episodes had no effect on memory. These results demonstrate that MS^{GABA} neuronal activity specifically during REMS is required for normal memory consolidation.

The physiological function of rapid eye movement sleep (REMS) is unclear (*1*). Evidence linking REMS to aspects of memory consolidation in mammals has been obtained using techniques such as statistical correlation, pharmacology, and REMS deprivation (*2*, *3*). However, whether REMS has a direct role in learning and memory remains controversial; correlative studies are not definitive, REMS has a transient pattern of occurrence that prevents REMS-selective pharmacological manipulation, and REMS deprivation has critical caveats that are difficult to fully control for (*4*, *5*).

During REMS in mice and rats, a prominent ~7-Hz theta oscillation is observed in local field potential (LFP) recordings from cortical structures, including the hippocampus (*6*, *7*). Hippocampal theta rhythms during REMS may contribute to memory consolidation by providing a mechanism for strengthening place cells formed during prior wakefulness (*8*, *9*). Theta rhythm generation requires an intact medial septum (MS) (*10*, *11*), although the MS is not involved in REMS generation itself (*12*, *13*). MS γ-aminobutyric acid–releasing (MS^{GABA}) neurons project to the hippocampus, probably pacing the hippocampal theta rhythm during REMS (*14*–*16*). In mice, we therefore used optogenetics to silence MS^{GABA} neurons and reduce theta activity selectively during REMS, without disturbing sleeping behavior, to determine whether intact MS^{GABA} neural activity during REMS is important for memory consolidation.

Adeno-associated virus (AAVdj) encoding Archaerhodopsin fused to an enhanced yellow fluorescent protein (eYFP) reporter (ArchT-eYFP) was injected into the MS of VGAT::Cre mice (Fig. 1A, top). The resulting ArchT-eYFP expression was ~95% specific for MS^{GABA} neurons (Fig. 1A, bottom, and fig. S1A), stable, and localized to the MS and the diagonal band of Broca (DBB) region for at least 3 months after injection. MS^{GABA} neural projections were observed throughout the hippocampus (Fig. 1B).

Whole-cell voltage and current clamp recordings of ArchT-eYFP–expressing MS neurons in acute brain slices (fig. S1B) revealed hyperpolarization (−39.9 ± 6.6 mV) and outward current (293.9 ± 69.2 pA) upon 594-nm light exposure (fig. S1B). Single-unit recordings in behaving transfected mice (fig. S1C) confirmed that photoinhibition during REMS, non-REM sleep (NREMS), and wakefulness rapidly produced a potent and reversible reduction in spiking of putative MS^{GABA} neurons (fig. S1D).

We next tested the effect of silencing MS^{GABA} neurons during REMS in freely behaving mice. Photoinhibition with constant light pulses delivered to the MS in ArchT-eYFP–expressing mice (ArchT mice) resulted in significantly (65.3 ± 5.6%) reduced theta power measured from dorsal hippocampal area CA1 LFP (CA1LFP) recording (Fig. 1D, top). No other frequency bands were affected, and the spectral profile of the CA1LFP returned to baseline levels almost immediately upon release of MS^{GABA} neurons from photoinhibition (Fig. 1D, top, and Fig. 2A). Current source density (CSD) analysis revealed that reduced theta power was present in all layers of dorsal hippocampal CA1 (Fig. 2B). Light pulses delivered to the MS of mice only expressing eYFP in MS^{GABA} neurons (YFP control mice) did not affect CA1LFP power (Fig. 1D, bottom), ruling out light as a potential confounding factor in these results. Inhibition of MS^{GABA} neurons did not perturb sleeping behavior (Fig. 1D, top), and the probability of state transition during REMS in ArchT mice was unaltered relative to YFP control mice (n = 30 ArchT mice, n = 19 YFP control mice; P = 0.63, unpaired Student's t test).

We optogenetically silenced MS^{GABA} neurons selectively during each REMS episode after acquisition of a novel object place recognition (NOPR) task (Fig. 3A). Mice showed no preference for either object during initial object habituation [day 1 (D1), task acquisition] (Fig. 3A, right). After acquisition, EEG/CA1LFP/EMG (EEG, electroencephalogram; EMG, electromyogram) activity was monitored for 4 hours. Upon entry into REMS, mice in the ArchT or YFP control group had light continuously delivered to the MS until transition to another state occurred, at which time light delivery ceased until subsequent REMS was detected (Fig. 3B). A group of ArchT-eYFP expressing mice that never received light (ArchT control) served as a baseline control for ArchT-eYFP transfection. To determine whether REMS was a critical factor in our results, a final group

[1]Integrated Program in Neuroscience, McGill University, Montreal, Quebec, Canada. [2]Department of Psychiatry, McGill University, Montreal, Quebec, Canada. [3]Department of Neurology and Department of Clinical Research, Inselspital University Hospital, University of Bern, Bern, Switzerland.
*Corresponding author. Email: sylvain.williams@douglas.mcgill.ca (S.W.); antoine.adamantidis@dkf.unibe.ch (A.A.) †These authors contributed equally to this work.

of mice expressing ArchT-eYFP (ArchT REM control) underwent the same protocol as mice in the ArchT group, with the exception that light delivery to the MS was delayed upon detection of REMS by ~5 min (supplementary methods). After the delay, light was delivered continuously to the MS for a duration equaling that of the preceding REMS episode. The result was a pattern of inhibition that, whereas statistically similar to the REMS-specific pattern that ArchT mice received, occurred primarily when mice were not engaged in REMS. MS^{GABA} neurons were inhibited during 91.6 ± 1.3% of the cumulative REMS duration occurring during the post-test period in ArchT mice (Fig. 3C, top, and fig. S3A), with little inhibition during other states (Fig. 3C, top; laser on 0.2 ± 0.0% of NREMS; 1.5 ± 0.2% of wakefulness). Sleep architecture was unaffected by REMS-selective MS^{GABA} neural photoinhibition during the 4-hour post-test period (fig. S3, A and B), and the only significant effect on the CA1LFP spectral profile (Fig. 3C, bottom, and figs. S4, A to C, and S5C) was reduced (60.2 ± 2.4%) REMS theta power. Basic firing activity during wakefulness, NREMS, and REMS of isolated single neurons recorded at the dorsal CA1 cell layer in a subset of mice during the 4-hour post-test period (supplementary methods) was unaffected by REMS-specific MS^{GABA} neural inhibition (fig. S6, A and B). Analysis of REMS immediately after the 4-hour post-test period when optogenetic silencing of MS^{GABA} neurons during REMS had ceased (4- to 5-hour post-test/recovery period) revealed an immediate return of REMS CA1LFP spectral power to baseline levels (fig. S4, B and C) and no alteration in cumulative and average episode durations in ArchT mice relative to controls (fig. S3C). EEG spindles (tables S1 to S3) and hippocampal ripples (tables S6 to S9) measured during NREMS throughout the course of the NOPR protocol were also unaltered.

On day 2 (D2), object 2 was moved to a new location while object 1 remained stationary (Fig. 3D, left). Because mice preferentially investigate novel stimuli, if object orientation memory is intact, mice should intrinsically investigate object 2 more than object 1 (*17*). Preference for object 2 [object 2 discrimination index (DI), supplementary methods] was not different relative to D1 testing in ArchT mice (Fig. 3D, right, and 3E). This result is not due to the MS light delivery method, because YFP control mice that underwent the same light delivery protocol (Fig. 3C, top; laser on 86.8 ± 4.6% of REMS; 0.2 ± 0.1% of NREMS; 2.7 ± 0.3% of wakefulness) had higher D2 object 2 DI relative to neutral D1 discrimination (Fig. 3D, right, and 3E). ArchT control mice also had increased object 2 DI during D2 testing from neutrality observed on D1 (Fig. 3D, right, and 3E). The co-occurrence of MS^{GABA} neural inhibition with REMS was a critical factor in the deficit observed in ArchT mice, because ArchT REM control mice demonstrated intact object recognition memory comparable to that of YFP control and ArchT control mice (Fig. 3D, right, and 3E). No evidence for differences in locomotion or motivation during testing were found between groups (fig. S5, A and B).

We next investigated whether normal contextual and emotional memory consolidation requires MS^{GABA} neural activity (Fig. 4). ArchT, YFP control, ArchT control, and ArchT REM control mice were fear-conditioned in a distinct context (context A) with three tone-shock events spanning a 9.5-min session. Freezing behavior between groups was not different during conditioning (Fig. 4A). For the subsequent 4 hours, a protocol similar to that used after D1 NOPR testing was again used

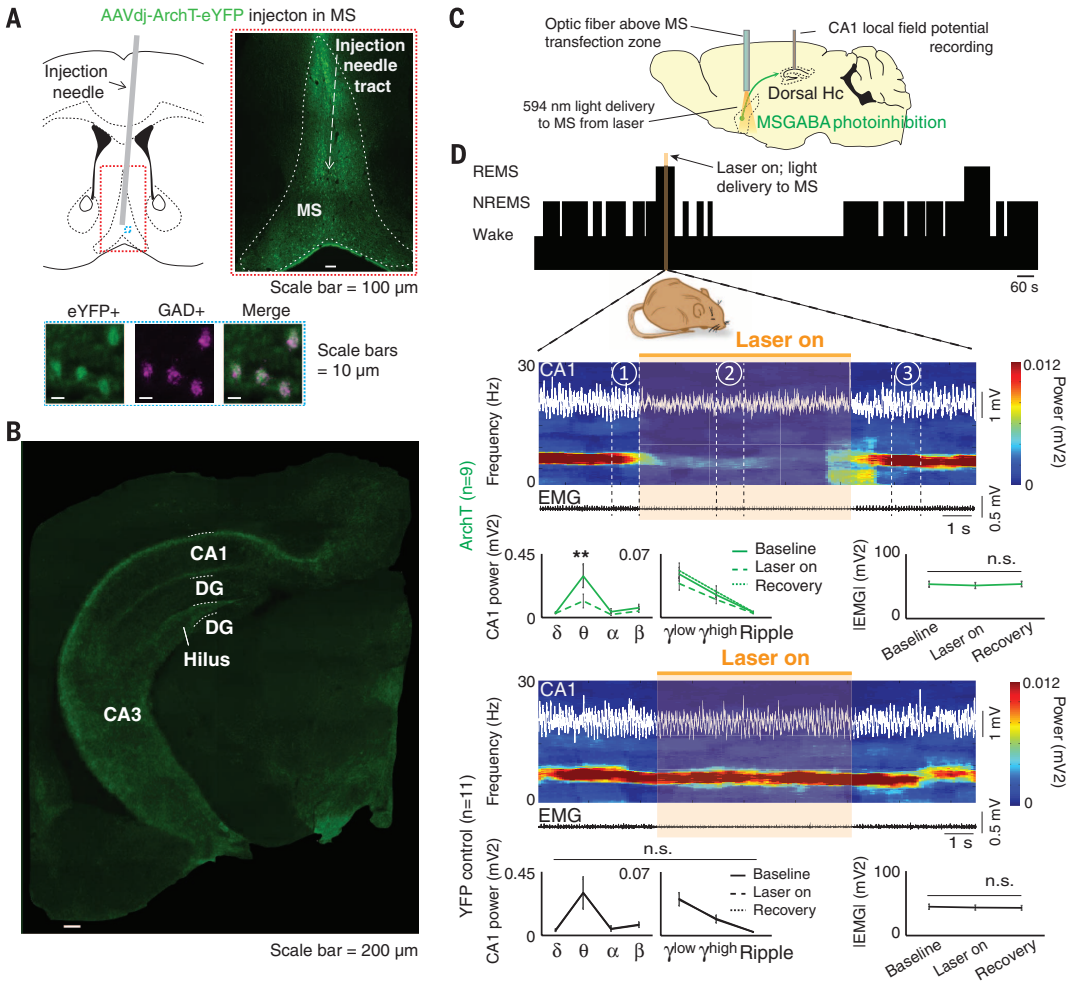

Fig. 1. ArchT-mediated inhibition of MS^{GABA} neurons during REMS reduces theta rhythm. (**A**) Schematic (top left) showing the MS injection site of Cre-dependent AAV in VGAT::Cre mice. After virus delivery, ArchT-eYFP is inverted in MS^{GABA} neurons, allowing transcription from the EF-1α promoter and subsequent expression of ArchT-eYFP to occur in the MS (top right). (Bottom) Cell-specific expression of ArchT-eYFP (green) in MS^{GABA} [glutamic acid decarboxylase (GAD^{+})] neurons (magenta) (quantified in fig. S1A). (**B**) Dense projections in the hippocampus originating from MS^{GABA} neurons (green). DG, dentate gyrus. (**C**) Schematic of the in vivo recording configuration; an optic fiber delivered orange laser light to the MS, allowing for optogenetic inhibition of MS^{GABA} neurons while recording the LFP signal from electrodes implanted in dorsal CA1. (**D**) Effect of MS^{GABA} neural inhibition during REMS on CA1LFP and EMG activity. Mice injected with a control virus resulting in expression of only eYFP in MS^{GABA} neurons controlled for the use of orange light (YFP control) [n = 9 for ArchT mice, n = 11 for YFP control mice; n.s. = not significant, $^{**}P < 0.01$, two-way analysis of variance (ANOVA) with Tukey post-hoc test].

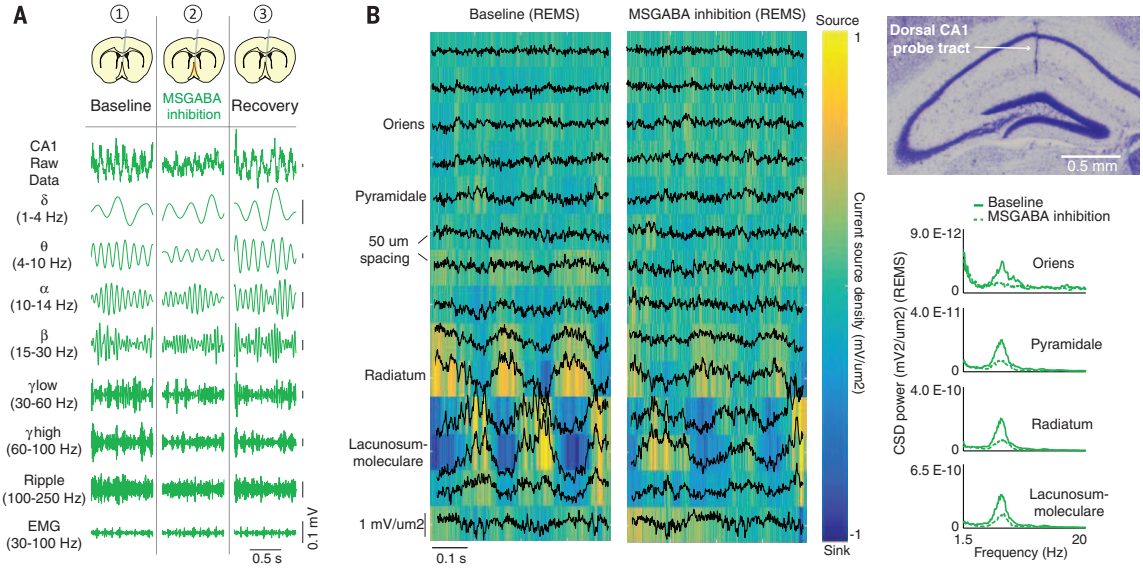

Fig. 2. MS^{GABA} neural silencing during REMS reduces theta power in all layers of dorsal hippocampal CA1. (**A**) Sample raw and filtered traces from ArchT example trace in Fig. 1D, as indicated. Recordings were from the stratum radiatum of dorsal hippocampal CA1. (**B**) (Left) CSD analysis completed on recordings obtained from dorsal hippocampal CA1 (top right) using a chronically implanted linear 16-channel probe (50 μm spacing between successive channels) during REMS under baseline and MS^{GABA} neural inhibition conditions. Graphs at right show layer-specific spectral analysis of CSDs for the baseline versus the MS^{GABA} neural inhibition condition (n = 1 AAVdj-ArchT–injected mouse).

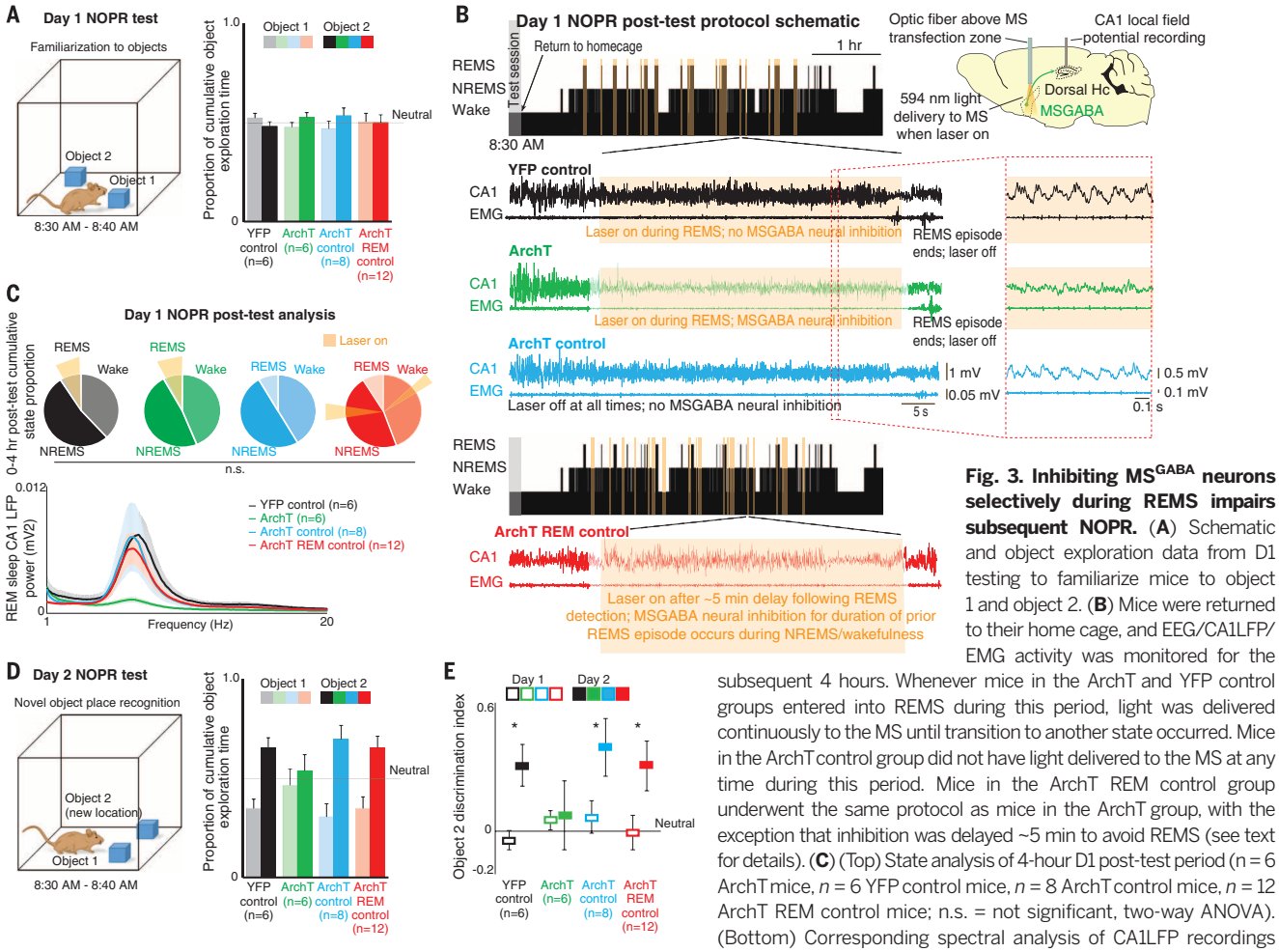

Fig. 3. Inhibiting MS^{GABA} neurons selectively during REMS impairs subsequent NOPR. (**A**) Schematic and object exploration data from D1 testing to familiarize mice to object 1 and object 2. (**B**) Mice were returned to their home cage, and EEG/CA1LFP/EMG activity was monitored for the subsequent 4 hours. Whenever mice in the ArchT and YFP control groups entered into REMS during this period, light was delivered continuously to the MS until transition to another state occurred. Mice in the ArchT control group did not have light delivered to the MS at any time during this period. Mice in the ArchT REM control group underwent the same protocol as mice in the ArchT group, with the exception that inhibition was delayed ~5 min to avoid REMS (see text for details). (**C**) (Top) State analysis of 4-hour D1 post-test period (n = 6 ArchT mice, n = 6 YFP control mice, n = 8 ArchT control mice, n = 12 ArchT REM control mice; n.s. = not significant, two-way ANOVA). (Bottom) Corresponding spectral analysis of CA1LFP recordings during REMS. (**D**) Schematic and object exploration data from D2 testing; only object 2 placement differed relative to D1. (**E**) Analysis of object 2 preference between D1 and D2 (n = 6 ArchT mice, n = 6 YFP control mice, n = 8 ArchT control mice, n = 12 ArchT REM control mice; *P < 0.05, paired Student's t test).

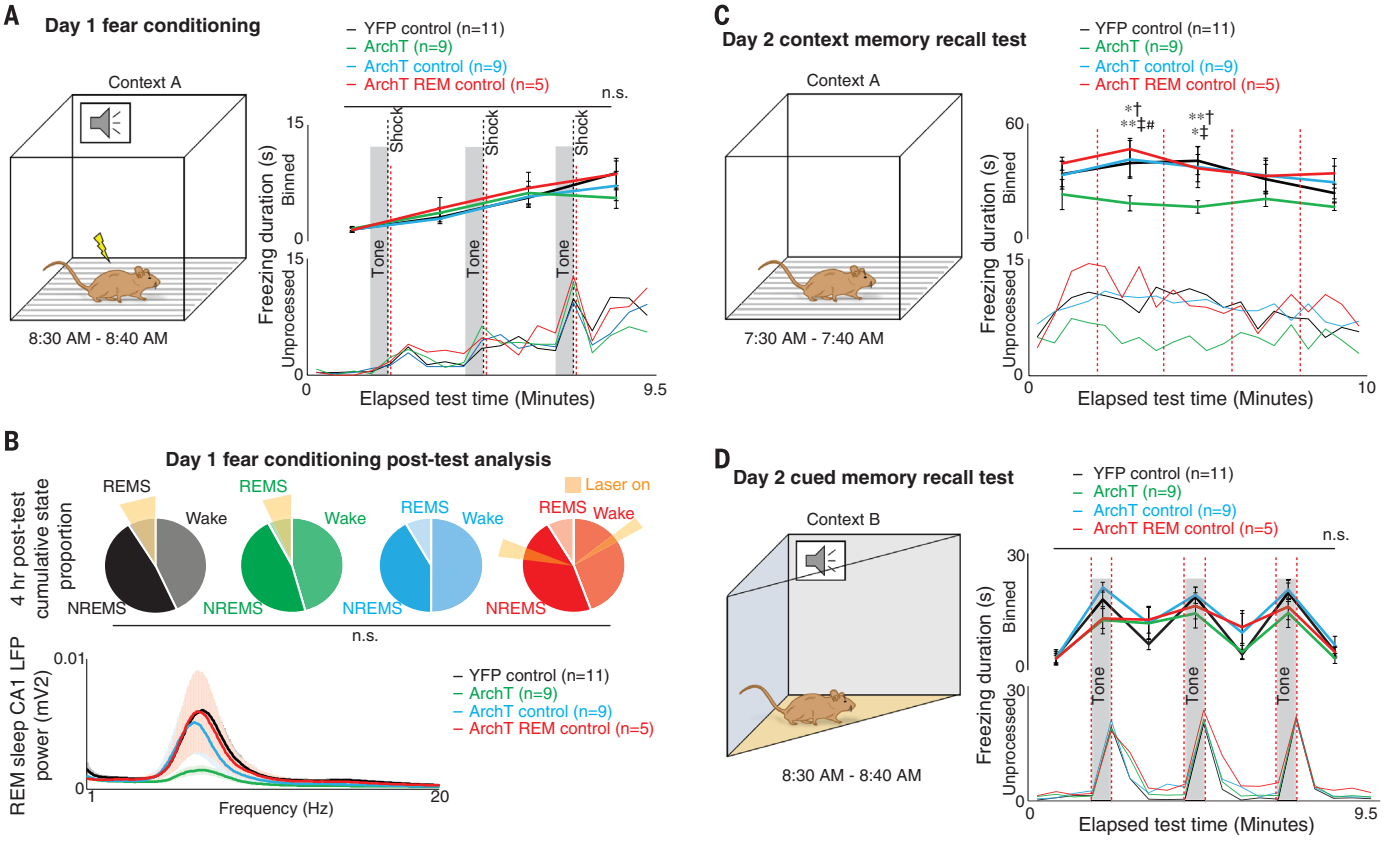

Fig. 4. Inhibiting MS^{GABA} neurons selectively during REMS after fear conditioning impairs contextual memory. (**A**) Fear conditioning schematic and freezing data. (**B**) Immediately after conditioning, mice were returned to their home cage, where they underwent the same procedure as that described after D1 NOPR testing (a full schematic is in Fig. 3B). (Top) State analysis of 4-hour post-conditioning period (n = 9 ArchT mice, n = 11 YFP control mice, n = 9 ArchT control mice, n = 5 ArchT REM control mice; n.s. = not significant, two-way ANOVA). (Bottom) Corresponding spectral analysis of CA1LFP recordings during REMS. (**C**) D2 contextual recall memory test schematic and freezing analysis. (**D**) D2 cued recall memory test schematic and freezing analysis. (A), (C), and (D) Freezing versus time graphs (n = 9 ArchT mice, n = 11 YFP control mice, n = 9 ArchT control mice, n = 5 ArchT REM control mice; n.s. = not significant, *P < 0.05, **P < 0.01, two-way repeated-measures ANOVA with Tukey post-hoc test; †YFP control versus ArchT mice, ‡ArchT control versus ArchT mice, #ArchT REM control versus ArchT mice). (A) and (D) Statistical results confirmed with Kruskal-Wallis test. Red lines indicate unprocessed data bin boundaries used for statistics (top right plot).

(see Fig. 3B for a detailed schematic). ArchT mice received selective MS^{GABA} neural inhibition during REMS (laser on 92.2 ± 2.2% of REMS; 0.2 ± 0.0% of NREMS; 1.6 ± 0.2% of wakefulness) during the 4-hour post–fear conditioning period (Fig. 4B). No difference in sleep-wake architecture (Fig. 4B, top, and fig. S7, A to C) or NREMS EEG spindle activity (tables S4 and S5) was found between groups, and the only significant effect on the CA1LFP spectral profile was a 57.8 ± 5.7% reduction in theta power in ArchT mice (Fig. 4B, bottom, and fig. S8, A to C).

The next day mice were first tested for contextual recall memory (Fig. 4C) followed by cued recall memory (Fig. 4D). Mice were placed in context A for 10 min, where conditioning had occurred the prior day, and allowed to move freely without any tone or shock. ArchT mice froze less than YFP control, ArchT control, and ArchT REM control mice (Fig. 4C, right). One hour later, mice were placed in a novel context (context B) for 9.5 min for cued recall testing, and a sequence of tones identical to those from prior fear conditioning was played. Freezing behavior was not different between the ArchT, YFP control, ArchT control, or ArchT REM control groups, with each group showing a robust freezing response selectively to the cue (tone) (Fig. 4D, right).

NOPR and fear-conditioned contextual memory in these experiments were probably hippocampus-dependent (*18*, *19*). Considering the potential importance of hippocampal REMS theta oscillations in processing place cell information (*8*, *9*), the impairments reported here could result from disrupted theta-dependent plasticity in hippocampal neurons during REMS after initial memory consolidation. REMS may also contribute to the homeostasis of network excitability (*20*, *21*). Disruption of hippocampal homeostasis could have contributed to the memory impairment we observed, although analysis of CA1 unit data did not reveal any clear indication of altered activity resulting from MS^{GABA} neural inhibition during REMS. Extrahippocampal inputs also must be considered, given known MS projection patterns (*22*). Indeed, current source density analysis from CA1 during REMS indicated a reduction in theta rhythm power at all layers upon MS^{GABA} neural inhibition. Thus, in addition to disrupted input from the Schaffer-collaterals, input from the entorhinal cortex via the perforant path was also disrupted. Given the importance of these inputs in spatial memory and hippocampal place cell activity (*18*, *23*), their disruption may be a mechanism involved in the blockade of consolidation we observed. In summary, our data provide experimental proof in a mouse model that MS^{GABA} neural activity occurring specifically during REMS after acquisition of a NOPR task or fear conditioning is critical for normal spatial and contextual memory consolidation.

REFERENCES AND NOTES

1. J. M. Siegel, *Nature* **437**, 1264–1271 (2005).
2. S. Diekelmann, J. Born, *Sleep* **11**, 114–126 (2010).
3. R. Stickgold, M. P. Walker, *Sleep* **28**, 1225–1227 (2005).
4. J. M. Siegel, *Science* **294**, 1058–1063 (2001).

5. R. P. Vertes, *Neuron* **44**, 135–148 (2004).
6. T. E. Robinson, R. C. Kramis, C. H. Vanderwolf, *Brain Res.* **124**, 544–549 (1977).
7. G. Buzsáki, *Neuron* **33**, 325–340 (2002).
8. G. R. Poe, D. A. Nitz, B. L. McNaughton, C. A. Barnes, *Brain Res.* **855**, 176–180 (2000).
9. K. Louie, M. A. Wilson, *Neuron* **29**, 145–156 (2001).
10. J. D. Green, A. A. Arduini, *J. Neurophysiol.* **17**, 533–557 (1954).
11. S. J. Mitchell, J. N. Rawlins, O. Steward, D. S. Olton, *J. Neurosci.* **2**, 292–302 (1982).
12. B. E. Jones, *Neuroscience* **40**, 637–656 (1991).
13. R. E. Brown, R. Basheer, J. T. McKenna, R. E. Strecker, R. W. McCarley, *Physiol. Rev.* **92**, 1087–1187 (2012).
14. H. Petsche, C. Stumpf, G. Gogolak, *Electroencephalogr. Clin. Neurophysiol.* **14**, 202–211 (1962).
15. A. P. Simon, F. Poindessous-Jazat, P. Dutar, J. Epelbaum, M. H. Bassant, *J. Neurosci.* **26**, 9038–9046 (2006).
16. K. Tóth, T. F. Freund, R. Miles, *J. Physiol.* **500**, 463–474 (1997).
17. M. Antunes, G. Biala, *Cogn. Process.* **13**, 93–110 (2012).
18. M. B. Moser, D. C. Rowland, E. I. Moser, *Cold Spring Harbor Perspect. Biol.* **7**, 1–15 (2016).
19. J. J. Kim, M. S. Fanselow, *Science* **256**, 675–677 (1992).
20. A. A. Borbély, *Hum. Neurobiol.* **1**, 195–204 (1982).
21. A. D. Grosmark, K. Mizuseki, E. Pastalkova, K. Diba, G. Buzsáki, *Neuron* **75**, 1001–1007 (2012).
22. R. C. Meibach, A. Siegel, *Brain Res.* **119**, 1–20 (1977).
23. M. E. Hasselmo, *Eur. J. Neurosci.* **28**, 1301–1315 (2008).

ACKNOWLEDGMENTS

We thank all members of the Williams and Tidis labs for their helpful comments on the manuscript, E. Boyden for viral constructs, and B. Lowell and L. Vong for mice. R.B. was supported by an Alexander Graham Bell Canada Graduate Scholarship [Natural Sciences and Engineering Research Council of Canada (NSERC)] while completing this research. S.D.G. was supported by a postdoctoral fellowship from Fonds de la Recherche en Santé du Québec. S.W. is supported by the Canadian Institutes of Health Research (CIHR) and NSERC. A.A. is supported by the Human Frontier Science Program (RGY0076/2012), the Douglas Foundation, McGill University, the Canadian Fund for Innovation (CFI), the Canadian Research Chair (CRC Tier 2), CIHR, NSERC, the Swiss National Science Foundation, the Inselspital, and the University of Bern. All data are available in the supplementary materials. We declare no conflicts of interest.

SUPPLEMENTARY MATERIALS

www.sciencemag.org/content/352/6287/812/suppl/DC1
Materials and Methods
Figs. S1 to S8
Tables S1 to S9
References (*24*–*27*)

9 October 2015; accepted 24 March 2016
10.1126/science.aad5252

ZIKA VIRUS

Zika virus impairs growth in human neurospheres and brain organoids

Patricia P. Garcez,[2,1]* Erick Correia Loiola,[1]† Rodrigo Madeiro da Costa,[1]† Luiza M. Higa,[3]† Pablo Trindade,[1]† Rodrigo Delvecchio,[3] Juliana Minardi Nascimento,[1,4] Rodrigo Brindeiro,[3] Amilcar Tanuri,[3] Stevens K. Rehen[1,2]*

Since the emergence of Zika virus (ZIKV), reports of microcephaly have increased considerably in Brazil; however, causality between the viral epidemic and malformations in fetal brains needs further confirmation. We examined the effects of ZIKV infection in human neural stem cells growing as neurospheres and brain organoids. Using immunocytochemistry and electron microscopy, we showed that ZIKV targets human brain cells, reducing their viability and growth as neurospheres and brain organoids. These results suggest that ZIKV abrogates neurogenesis during human brain development.

Primary microcephaly is a severe brain malformation characterized by the reduction of the head circumference. Patients display a heterogeneous range of brain impairments that compromise motor, visual, hearing, and cognitive functions (*1*).

Microcephaly is associated with decreased neuronal production as a consequence of proliferative defects and death of cortical progenitor cells (*2*). During pregnancy, the primary etiology of microcephaly varies from genetic mutations to external insults. The so-called TORCHS factors (toxoplasmosis, rubella, cytomegalovirus, herpes virus, and syphilis) are the main congenital infections that compromise brain development in utero (*3*).

[1]D'Or Institute for Research and Education (IDOR), Rio de Janeiro, Brazil. [2]Institute of Biomedical Sciences, Federal University of Rio de Janeiro, Rio de Janeiro, Brazil. [3]Institute of Biology, Federal University of Rio de Janeiro, Rio de Janeiro, Brazil. [4]Institute of Biology, State University of Campinas, Campinas, Brazil.
***Corresponding author. Email: ppgarcez@icb.ufrj.br (P.P.G.); srehen@lance-ufrj.org (S.K.R.)** †These authors contributed equally to this work.

An increase in the rate of microcephaly in Brazil has been associated with the recent outbreak of Zika virus (ZIKV) (*4*, *5*), a flavivirus that is transmitted by mosquitoes (*6*) and sexually (*7*–*9*). So far, ZIKV has been described in the placenta and amniotic fluid of microcephalic fetuses (*10*–*13*) and in the blood of microcephalic newborns (*11*, *14*). ZIKV had also been detected within the brain of a microcephalic fetus (*13*, *14*), and recently, direct evidence has emerged that ZIKV is able to infect and cause the death of neural stem cells (*15*).

We used human induced pluripotent stem (iPS) cells cultured as neural stem cells (NSCs), neurospheres, and brain organoids to explore the consequences of ZIKV infection during neurogenesis and growth with three-dimensional culture models. Human iPS-derived NSCs were exposed to ZIKV [multiplicity of infection (MOI), 0.25 to 0.0025]. After 24 hours, ZIKV was detected in NSCs (Fig. 1, A to D); viral envelope protein was evident in 10.10% (MOI, 0.025) and 21.7% (MOI, 0.25) of cells exposed to ZIKV (Fig. 1E). Viral RNA was also detected in the supernatant of infected NSCs (MOI, 0.0025) by quantitative reverse transcriptase polymerase chain reaction (qRT-PCR) (Fig. 1F), providing evidence of productive infection.

To investigate the effects of ZIKV during neural differentiation, mock- and ZIKV-infected NSCs were cultured as neurospheres. After 3 days in vitro (DIV), mock-infected NSCs generated round neurospheres. However, ZIKV-infected NSCs generated neurospheres with morphological abnormalities and cell detachment (Fig. 2B). After 6 DIV, hundreds of neurospheres grew under mock conditions (Fig. 2, C and E). In ZIKV-infected NSCs (MOI, 2.5 to 0.025), only a few neurospheres survived (Fig. 2, D and E).

Mock-infected neurospheres presented the expected ultrastructural morphology of the nucleus and mitochondria (Fig. 3A). Viral particles were present in ZIKV-infected neurospheres, similar to those observed in murine glial and neuronal cells (*16*). ZIKV was bound to the membranes and observed in mitochondria and vesicles of cells within infected neurospheres (arrows in Fig. 3, B and F). Apoptotic nuclei, a hallmark of cell death, were observed in all ZIKV-infected neurospheres that we analyzed (Fig. 3B). ZIKV-infected cells in neurospheres presented smooth membrane structures (Fig. 3, B and F), similar to other cell types infected with dengue virus (*17*). These results suggest that ZIKV induces cell death in human neural stem cells and thus impairs the formation of neurospheres.

To further investigate the impact of ZIKV infection during neurogenesis, human iPS-derived brain organoids (*18*) were exposed to ZIKV and observed for 11 DIV (Fig. 4). The growth rates of 12 individual organoids (six mock- and six ZIKV-infected) were measured during this period (Fig. 4, A to D). As a result of ZIKV infection, the average growth area of ZIKV-exposed organoids was reduced by 40% compared with brain organoids under mock conditions [0.624 ± 0.064 mm^2 for ZIKV-exposed organoids versus 1.051 ± 0.1084 mm^2 for mock-infected organoids (normalized); Fig. 4E].

Editor's Summary

Let sleeping mice remember

The role of REM (rapid eye movement) sleep for memory consolidation has been discussed for a long time. Boyce *et al.* used optogenetics to inhibit theta oscillations in the mouse hippocampus during REM sleep (see the Perspective by Kocsis). Both object recognition memory and contextual fear memory were impaired. This consolidation mechanism occurred in a critical time window immediately after training. Disrupting the same system for similar durations during non-REM sleep or wakefulness had no effect on memory.

Science, this issue p. 812; see also p. 770

www.sciencemag.org/content/352/6287/812/suppl/DC1

Supplementary Materials for

Causal evidence for the role of REM sleep theta rhythm in contextual memory consolidation

Richard Boyce, Stephen D. Glasgow, Sylvain Williams,*Antoine Adamantidis*

*Corresponding author. Email: sylvain.williams@douglas.mcgill.ca (S.W.);
antoine.adamantidis@dkf.unibe.ch (A.A.)

Published 13 May 2016, *Science* **352**, 812 (2016)
DOI: 10.1126/science.aad5252

This PDF file includes:

Materials and Methods

Animals

VGAT-ires-Cre (VGAT::Cre) transgenic mice (The Jackson Laboratory, stock number 016962) were used in all experiments in order to selectively target Cre recombinase expression to GABAergic neurons. For the collection of *in vivo* data only male mice were used, whereas both females and males were used for the collection of *in vitro* slice electrophysiology data as well as data for FISH experiments. Mice were housed individually in polycarbonate cages at constant temperature (22° C) and humidity (30-50%) and were kept on a regular circadian cycle (12 h:12 h light:dark cycle, lights on at 7:30 a.m.). Mice were provided with food and water ad libitum. Animals were treated according to protocols and guidelines approved by McGill University and the Canadian Council of Animal Care.

Virus-mediated targeting of opsin and eYFP expression

At ~10 weeks age, male VGAT::Cre mice to be used for *in vivo* behavioral testing were anesthetized with isoflurane (5% induction, 1-2% maintenance). 0.6 µL of recombinant AAVdj carrying either Ef1α-DIO-ArchT-eYFP or control Ef1α-flex-eYFP (plasmids were provided by Dr. K. Deisseroth; viral vectors were packaged at Vollum Vector Core, University of Washington, Washington, USA) were stereotaxically injected into the medial septum (MS) (anteroposterior (AP), +0.86; mediolateral (ML), 0.0; dorsoventral (DV), -4.5; all coordinates relative to Bregma) through a 28 G cannula at a rate of 50 ηL/min. The injection needle was lowered through a hole drilled lateral to the midline (AP, +0.86; ML, -0.5) at an angle of ~6.4 ° (in the ML axis) relative to the vertical plane in order to avoid the sagittal sinus. For mice that were injected for use in *in vitro* experiments the same procedure was followed, however injections were performed at ~2 weeks of age.

Fluorescent in situ hybridization (FISH) for quantification of construct targeting specificity

Mice that had been injected at least 1 month prior were deeply anesthetized with isoflurane and subsequently decapitated. The brain was quickly removed and rapidly frozen in methyl-butane (-80 º C). Brains were sectioned at 16 µm thickness using a cryostat and subsequently mounted on RNAase-free glass slides. Slides were first incubated for 20 minutes in filtered 4 % PFA in 1 x PBS made with distilled water containing 0.1% Diethyl pyrocarbonate (DEPC water). This was followed by a wash in PBS and subsequent incubation for 10 minutes in 0.3 % H_2O_2 in PBS, followed by another wash in PBS. Slides were then rinsed in DEPC water before undergoing a 10 minute acetylation in 0.1 M (Tris-acetate EDTA) (TEA) buffer (TEA in DEPC water with 25 % acetic anhydride). Slides were next washed 5 x 5 minutes in 1 x PBS followed by a series of 90 s dehydrations in ethanol (60 %, 80 %, 95 %, 100%) mixed in DEPC water. After allowing the slides to air-dry for 10 minutes the sections on the slides were circumscribed with an immEdge pen. The sections on the slides were then incubated for 2 h at 60 º C with 300 µL/slide of hybridization buffer (40 % deionized formamide, 10 mM Tris-HCl (pH 8.0), 200 µg/mL yeast tRNA, 10 % dextran sulfate, 1 x Denhardt's solution, 600 mM NaCl, 1 mM EDTA (pH 8.0) dissolved in H2O). Afterwards, the riboprobe was diluted 1:500 in hybridization buffer and 300 µL of solution was applied

to sections on each slide. The slides were then coverslipped and incubated for 12 h at 60 º C in a humid chamber. The following day, slides were first washed 5 x 5 minutes in 5x SSC (diluted in sterile H20) at 60 º C followed by a 1 minute wash in 2x SSC at 60 º C. A wash for 30 minutes at 60 º C in 0.2x SSC/Formamide (40%) was completed next, followed by two 5 minute washes in 0.2 x SSC and 1x PBS at room temperature. Slides were then blocked in 4 % BSA and 0.5 % blocking reagent in 1x PBS for 1 h. Sections on slides were then covered in rabbit anti-GFP diluted 1:2000 in PBST-BSA 4%, coverslipped, and incubated for 36 h at room temperature. After incubation in the primary antibody, slides were washed 5 x 5 minutes in 1x PBS and subsequently covered in 300 µL sheep anti-DIG-POD diluted 1:500 in 1x PBS, coverslipped, and incubated for 6 h at room temperature. Another 5 x 5 minute wash in 1x PBST was completed after, followed by application of 200 µL TSA-cy3 diluted 1:100 in amplification buffer over sections on each slide which were subsequently coverslipped and incubated for 10 minutes. The slides were then washed 5 x 5 minutes in PBST and sections on each slide were subsequently covered with alexa fluor 488 ex anti-rabbit IgG (H+L) 1:200 in PBST, coverslipped and incubated for 1 h at room temperature. Slides then underwent 3 x 5 minute washes in 1 x PBST and 5 x 5 minutes in 1 x PBS before finally being covered in Fluoromount and permanently coverslipped. Fluorescent images from immunolabelled sections were collected using a fluorescent microscope; quantification of colocalization was completed on sections containing the MS.

In vitro electrophysiology experiment preparation

Three to five weeks following virus injection, mice were deeply sedated using isoflurane, decapitated, and the brain was rapidly removed and cooled in ice-cold high-sucrose cutting solution containing (in mM): 252 sucrose, 26 NaHCO3, 2.5 KCl, 4 MgCl2, 1.25 KH2PO4, 0.1 CaCl2 and 10 glucose. All mice were sacrificed during the light phase of the sleep-wake cycle and recordings were performed in late morning and early afternoon. Coronal slices were cut using a vibratome and allowed to recover for ~1.5 h at 22 ± 0.5 º C in artificial cerebrospinal fluid (ACSF) containing (in mM): 124 NaCl, 5 KCl, 1.25 NaH2PO4, 2 MgSO4, 2 CaCl2, 26 NaHCO3, and 10 dextrose saturated with 95 % 02 and 5 % CO2 (pH ~7.3, 300-310 mOsm). Individual brain slices were then transferred to the recording chamber and perfused continuously with oxygenated ACSF (1.5-2 mL min-1) maintained at 22 ± 0.5 º C. Cellular morphology and fluorescence were visualized with an upright fluorescent microscope equipped with a 40x water-immersion objective, differential interference contrast optics, infrared differential interference contrast and a near-infrared fluorescence camera.

In vitro electrophysiology experiment recording and analysis

Micropipettes were prepared from borosilicate glass capillaries (1.0 mm outer diameter, 0.58 mm inner diameter) using a horizontal puller, and had tip resistances of 3-8 MΩ. Tight gigaohm seals (>1 GΩ) were obtained under voltage clamp by applying gentle negative pressure, and whole-cell configuration was achieved using strong negative pressure. Somatic whole-cell current and voltage-clamp recordings from YFP-expressing medial septal neurons were obtained using patch recording pipettes containing (in mM): 120 K-gluconate, 20 KCl, 10 N-2-hydroxyethylpiperazine-N′-2-ethanesulfonic acid (HEPES), 7 phosphocreatine di-Tris, 2 MgCl2, 0.2 ethylene glycol-bis (β-aminoethyl ether)-N,N, N′, N′-tetraacetic acid (EGTA), 4 Na2+-ATP, and 0.3 GTP-Tris (pH adjusted to 7.20-7.26 using KOH, 275-85 mOsm). Series resistances were

continuously monitored using a brief 5 mV depolarizing voltage step and data were discarded if intrinsic cell properties (resting membrane potential, input resistance) were more than 3 s.d. outside of the group mean and/or access resistance changed by >15 %. An Axopatch 700B amplifier was used for all current-clamp and voltage-clamp recordings and signals were digitized and sampled at 20 kHz for storage on a hard-disk. Current-clamp recordings were filtered at 10 kHz, and voltage-clamp data were filtered at 2 kHz.

For optogenetic inhibition, square pulses of orange (594 nm) light were delivered using lasers connected to a 200 µm optical fiber and triggered via a built-in transistor-transistor logic (TTL) circuit. Light intensity was tested before each experiment, and was calibrated to emit 20 mW from the tip of the optical fiber.

Electrophysiological characteristics of VGAT neurons were quantified using Clampfit 10.3 software package. Action potential measurements were derived from the first spike in response to a depolarizing intracellular current injection (typically 40-60 pA), and action potential amplitude was calculated from resting membrane potential. Action potential duration and afterhyperpolarizations were calculated from action potential threshold, and input resistance and rectification ratio was calculated in response to a -100 pA and -200 pA hyperpolarizing current pulse, respectively, from a holding voltage of -60 mV.

Electrode construction for *in vivo* experiments

Tetrodes were composed of 17.5 µm diameter platinum-iridium wire (platinum:iridium 90%:10%) with Teflon and VG bond coating for insulation and heat-induced annealing, respectively. Tetrodes were constructed by twisting together 4 wires followed by briefly heating one end of the tetrode to anneal the VG bond coating on each wire together without damaging the Teflon insulation. Individual wire leads from the non-annealed end were then soldered onto an electrode interface board. For hippocampal area CA1 (CA1) recordings 3 tetrodes were arranged in a linear array (0.4 mm spacing between adjacent tetrodes). Epoxy was used to cement tetrodes in the correct orientation for implantation and also served to insulate any exposed wire at the connection point with the electrode interface board. The annealed tip of each tetrode in the array was cut to equal length using sharp scissors and the cut tetrode ends were cleaned immediately prior to surgery to give an impedance of ~1 MΩ.

Electrode and optic fiber implantation for *in vivo* experiments

At ~ 18 weeks mice injected for *in vivo* experiments were anesthetized with isoflurane (5% induction, 0.5-2% maintenance). The skull was completely cleared of all connective tissue and thoroughly dried using alcohol. To facilitate light delivery to the transfection zone within the MS, a hole was drilled in the skull above and lateral to the medial septum (AP, +0.86; ML, -0.5). After gently cutting through the dura an optic fiber implant, constructed by cementing a cleaved piece of optic fiber ~ 12 mm in length into a ceramic ferrule, was lowered through the hole at an angle of ~4.5 ° (in the ML axis) with the optic fiber end location targeted just above the medial septum (AP, +0.86; ML, -0.2; DV, -3.83). For 'optrode' (optic fiber + tetrode) recordings the optic fiber was positioned as described above, however a tetrode was cemented to the optic fiber, with the tetrode tip extending ~0.8 mm beyond the tip of the optic fiber. For CA1 tetrode placement, holes were drilled through the skull above the dorsal hippocampus (AP, -2.45; ML, +1.4, 1.8, 2.2). After gently cutting the dura, the tetrode array was slowly lowered

1.3 mm (relative to Bregma) with the end target being deep stratum radiatum of the dorsal CA1 region. For 16-channel (50 µm site spacing oriented vertically) silicon probe implantation spanning CA1, the same procedure was used with slightly different coordinates (probe tip target: AP, -2.45; ML, +1.50; DV, – 1.50). An EEG screw was placed in the skull above the hippocampus in the contralateral hemisphere (AP, -2.3; ML, -1.35). 2 EMG electrodes consisting of stranded tungsten wires inserted into the neck musculature were used to record postural tone. Screws placed in the bone above the frontal cortex and cerebellum served as ground and reference, respectively. Following optic fiber, electrode, ground and reference placement, dental cement was applied to secure the implant permanently to the skull.

Post-surgery habituation to recording setup

Following surgery, mice were allowed to recover undisturbed for at least 1 week. Once mice had recovered from surgery they were briefly anesthetized with isoflurane (5% induction, 2% maintenance) and a custom built headstage pre-amplifier tether was attached to a connector on the top of the implanted electrode interface board. An optic fiber patch cord assembled in-house using a standard kit was connected to the exposed end of the optic fiber implant. Black nail polish was applied to the entire implant as well as the initial portion of the optic fiber patch cord to reduce the amount of light emanating from the implant and therefore prevent excessive disruption of mice from escaping light when the laser was on. Mice were then returned to their home cage and were left undisturbed until they were habituated to being chronically tethered and exhibited a regular sleep-wake cycle; typically 5 to 7 days.

In vivo electrophysiological recording

Recordings began only after mice were habituated to being chronically tethered. All recorded signals from implanted electrodes were amplified by the headstage pre-amplifier tether before being digitized at 16000 Hz using a digital recording system and saved to a hard disk.

Light delivery to the MS *in vivo*

For optical experiments, orange (594 nm wavelength) light was delivered to the MS from a TTL controlled laser with adjustable output intensity via the optic fiber patch cord-optic fiber implant system. For each AAVdj-ArchT-transduced mouse, the minimum amount of light estimated to be present at the tip of the optic fiber implant required to produce maximal effects on the CA1 theta rhythm during REM sleep (REMS) was determined before behavioral experiments were started in order to minimize unwanted side-effects including light-induced tissue damage as well as excessive disturbance of animals. The estimation was based on pre-surgery testing of transmittance of light through the optic fiber patch cord and optic fiber implant. The estimated amount of light determined using these criteria rarely exceeded 20 mW, and was never allowed to exceed 30 mW. The amount of light that each control AAVdj-eYFP-injected mouse received during all optical experiments was matched with an AAVdj-ArchT-injected mouse.

Baseline recording and characterization of optical inhibition *in vivo*

Prior to any optical testing or behavioral experiments a 24 h baseline recording was performed to ensure that every mouse demonstrated a regular sleep-wake cycle. Afterwards, baseline optical testing was completed. This consisted of no fewer than 10 relatively brief (5-10 s) isolated periods of light delivery to the MS during REMS as well

as NREMS and active wakefulness to determine both the basic effects of optical inhibition of MS GABAergic (MS^{GABA}) neurons, as well as to calibrate the appropriate amount of light intensity to use for subsequent behavioral experiments as discussed above. Once the baseline recording and baseline optical testing were completed, behavioral experiments commenced. AAVdj-ArchT-injected mice were randomly assigned to either the test (ArchT) or control (ArchT control or ArchT REM control) condition at this time. All AAVdj-eYFP-injected mice were placed in the YFP control group.

Novel object place recognition procedure and behavioral analysis

For all mice the first behavioral experiment to be completed was a novel object place recognition task, a modified version of the novel object recognition task (*17*). The test area consisted of a 30.5 cm^3 open-topped square container. The bottom and walls of the container were painted with white waterproof paint and unique black patterns were present on each of the 4 walls. The test was run on 3 consecutive days within the first two hours of light cycle onset (7:30 a.m. to 9:30 a.m.) in a room separate from the room in which the home cage was located. The precise test time for each mouse was kept consistent for each of the 3 days. On the first day of testing (test area habituation/baseline (Day 0)), mice were placed in the empty test area and allowed to explore freely for 10 minutes before being returned to their home cage. For the second day of testing (Day 1), 2 identical yet individually identified objects (Object 1 and Object 2) were each placed in a randomly assigned quadrant within the test area and mice were again allowed to explore freely for 10 minutes before being returned to their home cage. Upon being placed back in their home cage, EEG, CA1 LFP (CA1LFP) and EMG activity was manually monitored by an experimenter continuously for 4 hours. The real-time behavioral state was determined based on criteria discussed below for vigilance state architecture analysis. Whenever mice in either the ArchT or YFP control groups entered into REMS during the 4 h post-test period, the laser was manually activated and orange laser light was continuously delivered to the MS via the optic fiber patchcord/implant system until the mouse transitioned out of REMS, at which time the laser was turned off until the next REMS episode occurred. An ~10 s delay existed for manual detection of REMS to ensure that mice were in stable REMS. For mice in the ArchT REM control group each REMS episode occurring during the 4 h post-test period was manually documented and the duration noted; however, delivery of laser light to the MS did not occur immediately upon detection of REMS but was instead delayed by ~5 min from the end of the REMS episode. Following the delay laser light was delivered continuously to the MS for a timespan equal to the duration of the preceding REMS episode, unless the rare event of a mouse transitioning to REMS while the laser was on occurred, in which case the laser was turned off. This method was effective in providing a pattern of MS^{GABA} neural photoinhibition that, while statistically the same as that provided selectively during REMS to mice in the ArchT group, almost entirely avoided REMS in the ArchT REM control group of mice. Mice in the ArchT control group did not have light delivered to the MS at any point during behavioral testing. On the third and final day of testing (Day 2) the same 2 identical objects were placed within the test area as done on the day prior with the exception that Object 2 was located in a different quadrant relative to Day 1 position. Mice were given 10 minutes to explore the test area before being returned to their home cage. For each day of testing recordings were obtained from

electrodes during the testing period in addition to the first 5 hours after the mouse had been returned to its home cage immediately following the conclusion of testing. Both the test area and each of the identical objects used in this task were thoroughly washed with Peroxyguard before every test session. Test sessions on each day were recorded with an overhead video camera. For analysis of novel place recognition data, the time spent exploring each object during the test period was measured for each mouse on Day 1 and Day 2 of testing. For statistical analysis, the preference of mice for Object 2 exploration was determined by the following equation:

Object 2 discrimination index (DI)= ((Object 2 exploration (s)-Object 1 exploration (s)))/((Object 2 exploration (s)+Object 1 exploration (s)))

Movement data for mice during each test session was completed through analysis of video recordings from each test session at 1 Hz resolution using custom scripts in Matlab.

Fear conditioning procedure and behavioral analysis

For all mice the second and final behavioral task completed involved testing context- and cue-based responses following a standard fear conditioning protocol (*24*). Testing was completed over two days and always took place within the first 2 hours of the onset of the light cycle (7:30 a.m. to 9:30 a.m.) in a room separate from the room in which the home cage was located. On the first day of testing each mouse underwent the fear conditioning protocol. The floor of the test area consisted of a metal grid through which electrical current could be applied, while the wall panels were composed of opaque white Plexiglas with distinct black markings. The roof panel of the test area was composed of transparent Plexiglas to allow mouse behavior to be recorded with a video camera. A hole in the roof panel allowed the mouse to remain tethered during testing. The conditioning protocol consisted of three 80 dB tones 28 s in duration that were each immediately followed by 2 s of 0.5 mA current delivery through the metal grid floor. Each 30 s tone-shock event was immediately preceded and followed by 120 s blocks of time in which no tone or shock was present. Thus the total test time was 9.5 minutes. Once testing was complete, mice were immediately returned to their home cage. Between each conditioning session the test area was cleaned thoroughly with Peroxyguard. Upon being placed back in their home cage, EEG, CA1LFP and EMG activity was continuously monitored for 4 hours. The laser delivery protocol was the same for each group during the 4 h post-fear conditioning period as for the Day 1 post-test period for novel object place recognition testing discussed in the prior section. The second and final day of testing consisted of contextual and cued memory recall tests that were each completed 1 h apart but both within the first 2 hours of the onset of the light cycle (7:30 a.m. to 9:30 a.m.). For the context test, the exact same test area setup (context A) and test duration (9.5 min) that was used for fear conditioning on the prior day was again used, however no tone-shock events were present. Upon test completion, mice were immediately returned to their home cage for ~1 h until the cue test commenced. The test area was thoroughly cleaned with Peroxyguard between subsequent test sessions. For the cue testing the test area (context B) was substantially different than that used for the conditioning session and context testing. The floor consisted of a black Plexiglas panel covered in woodchip bedding, the walls were black Plexiglas, the shape of the testing area had a triangular configuration as opposed to the square configuration used for fear conditioning and context testing, and 70% ethanol was used to clean the test area between mice as opposed to Peroxyguard. During the cue test

three 80 dB tones 28 s in duration, identical to those produced during fear conditioning in context A the prior day, were evenly spaced over a 9.5 minute test period. EEG, CA1LFP and EMG recordings were made for 5 hours continuously following fear conditioning, and 1 h following completion of cue testing the following day. Test sessions on each day were recorded with a video camera. For the fear conditioning and subsequent contextual and cued recall memory test sessions, fear response was assessed by quantifying observed freezing behavior (*25*), identified as absence of movement except for breathing, in 30 s bins covering the entire duration of each test session (titled 'unprocessed' freezing analysis in figures). For statistical analysis of freezing behavior, data was further binned as described in the text and accompanying figures (titled 'binned' freezing analysis in figures).

Vigilance state architecture analysis

For all recordings made during behavioral testing, EEG, CA1LFP and EMG data were plotted and the vigilance state was manually scored in 5 s epochs using a custom written Matlab program. Scoring was based on visual characteristics of the CA1LFP, EEG and EMG data, fast Fourier transform analysis of each epoch scored as well as video monitoring of mouse behavior. Wakefulness was defined by a de-synchronized low-amplitude EEG and CA1LFP and tonic EMG activity with periods of movement-associated bursts of EMG activity. NREMS was defined as synchronized, high amplitude, low-frequency (δ, 1-4 Hz) EEG and CA1LFP activity that was accompanied by reduced EMG activity relative to that observed during wakefulness. REMS was defined as having reduced δ power, a prominent theta rhythm (4-10 Hz) and an absence of tonic muscle activity. In cases where theta power was significantly reduced during REMS due to photoinhibition, reduced δ power, lack of EMG tone and observation of sustained quiescent behavior were found to be highly reliable indicators of ongoing REMS. Hypnogram analysis (cumulative duration and average episode duration for each vigilance state) was completed using custom scripts in Matlab.

Electrophysiological analysis of in vivo MS unit, CA1 unit, EEG, CA1LFP and EMG data

All electrophysiological analysis was completed using custom scripts in Matlab unless otherwise noted.

For recording unit activity in the MS and CA1 pyramidal cell layer, single units were manually isolated from 600 – 6000 Hz filtered tetrode recordings using the clustering method (50 μV spike detection threshold) with criteria similar to what has been discussed elsewhere (*26*). Briefly, only units that formed clusters with clear boundaries were used for subsequent analysis. Additional requirements for single units included stability for the duration of recording and the presence of a clear refractory period of at least 3 ms between subsequent spikes determined through inter-spike interval analysis. Once sorting was complete, timestamp and spike waveform data of isolated units was output into Matlab for further analysis. For units isolated at the CA1 pyramidal cell layer, analysis for each treatment group revealed a minority (~3 %) of units possessing a symmetrical as opposed to unsymmetrical waveform which has previously been used as a method to identify putative interneurons and pyramidal cells, respectively (*26*). However, due to the low n analysis of symmetrical units was severely restricted. Thus, symmetrical units were removed from further analysis and all data shown was obtained from isolated units with unsymmetrical waveforms. Analysis was only completed on unit

data recorded during novel object place recognition testing as there was an insufficient number of stable units contained within the fear conditioning data.

Current source density (CSD) (*27*) was calculated from 16-channel silicon probe LFP recordings using the following equation:

$CSD(x,t) = (\sigma(2(x,t)-(x+\Delta x,t)-(x-\Delta x,t))/((\Delta x)^2)$

where (x,t) is the potential at depth x for time point t, with Δx of 50 μm. Conductivity (σ) was assumed constant and units for CSD are reported as mV/ μm2.

Vigilance state-specific spectral analysis of CA1LFP and CSD data was completed using inputs from the Chronux signal processing toolbox (window size = 5 s, step size = 5 s, tapers [3 5]). Analysis for each mouse was completed using the best (optimal combination of stability and size) individual electrode from the most accurately placed tetrode determined histologically (described further below). Analysis of EMG activity was completed by applying a 100 Hz high-pass filter to the data and subsequently integrating the rectified signal over 5 s windows.

Detection of transient EEG spindle and CA1LFP ripple activity during NREMS was completed on 30s windows of continuous NREMS that occurred during the recording period; there was no overlap in subsequent analysis windows. For each window, the signal was first bandpass filtered (EEG/spindle, 9-15 Hz; CA1LFP/ripple, 100-250 Hz) and the absolute amplitude was calculated with set resolution within the analysis window (EEG/spindle, 100 ms; CA1LFP/ripple, 10 ms). The mean and standard deviation (SD) for the absolute amplitude was calculated and the detection threshold was set at 1.5 SD above the mean for spindle analysis and 3 SD above the mean for CA1LFP ripple analysis. Values for detection threshold were selected based on accuracy of automatic detection as compared to manual scoring. EEG spindles and CA1LFP ripples were identified from detected above threshold data time points using additional criteria (EEG/spindle, minimum duration between successive spindles = 0.5 s, maximum duration of spindle = 3 s; CA1LFP/ripple, minimum duration between successive ripples = 30 ms).

Histological confirmation of electrode/optic fiber placement and construct expression

Following completion of all behavioral experiments, mice were deeply anesthetized with ketamine/xylazine/acepromazide (100, 16, 3 mg/kg, respectively, intraperitoneal injection). Electrode sites were marked by passing a current of 10 μA for ~20 s through each of the CA1 electrodes. Mice were then perfused transcardially with 1 x PBS-heparine 0.1%, pH 7.4, followed by 4% paraformaldehyde in PBS (PFA). The brains were then extracted and postfixed overnight in PFA at 4 º C and subsequently cryoprotected in 30% sucrose dissolved in PBS for an additional 24 h at 4 º C. Each brain was then frozen and sectioned at 50 μm using a cryostat; odd sections were collected, mounted on glass slides and stained with cresyl violet prior to being coverslipped for confirmation of electrode and optic fiber placement. To confirm construct expression, even sections were first washed in PBS 1x-Triton (0.3 %) (PBST), incubated in blocking solution (4 % bovine serum albumin (BSA) in PBST) for 60 minutes at room temperature and subsequently incubated in rabbit anti-GFP diluted 1:5000 in 4 % BSA overnight at 4 º C. Sections were then incubated in alexa fluor 488 ex anti-rabbit IgG (H+L) diluted 1:1000 in PBST to detect the primary antibody for 1 h at room temperature and then mounted on glass slides and permanently coverslipped with Fluoromount-G. Images of cresyl violet stained sections were obtained using a light

microscope whereas fluorescent images from immunolabelled sections were collected using a fluorescent microscope. Only mice with histologically confirmed placement of at least 1 tetrode in deep CA1 stratum radiatum and optic fiber placement as well as proper construct expression in the MS were used in the present study. Additionally, only mice with histologically confirmed placement of at least 1 tetrode in the CA1 pyramidal cell layer were further considered for analysis of CA1LFP ripple and unit activity.

Statistical analysis

Statistical analysis was performed using GB-Stat. All data are presented as mean ± standard error of the mean (SEM) and statistic test details are described in the text. $P < 0.05$ was considered statistically significant.

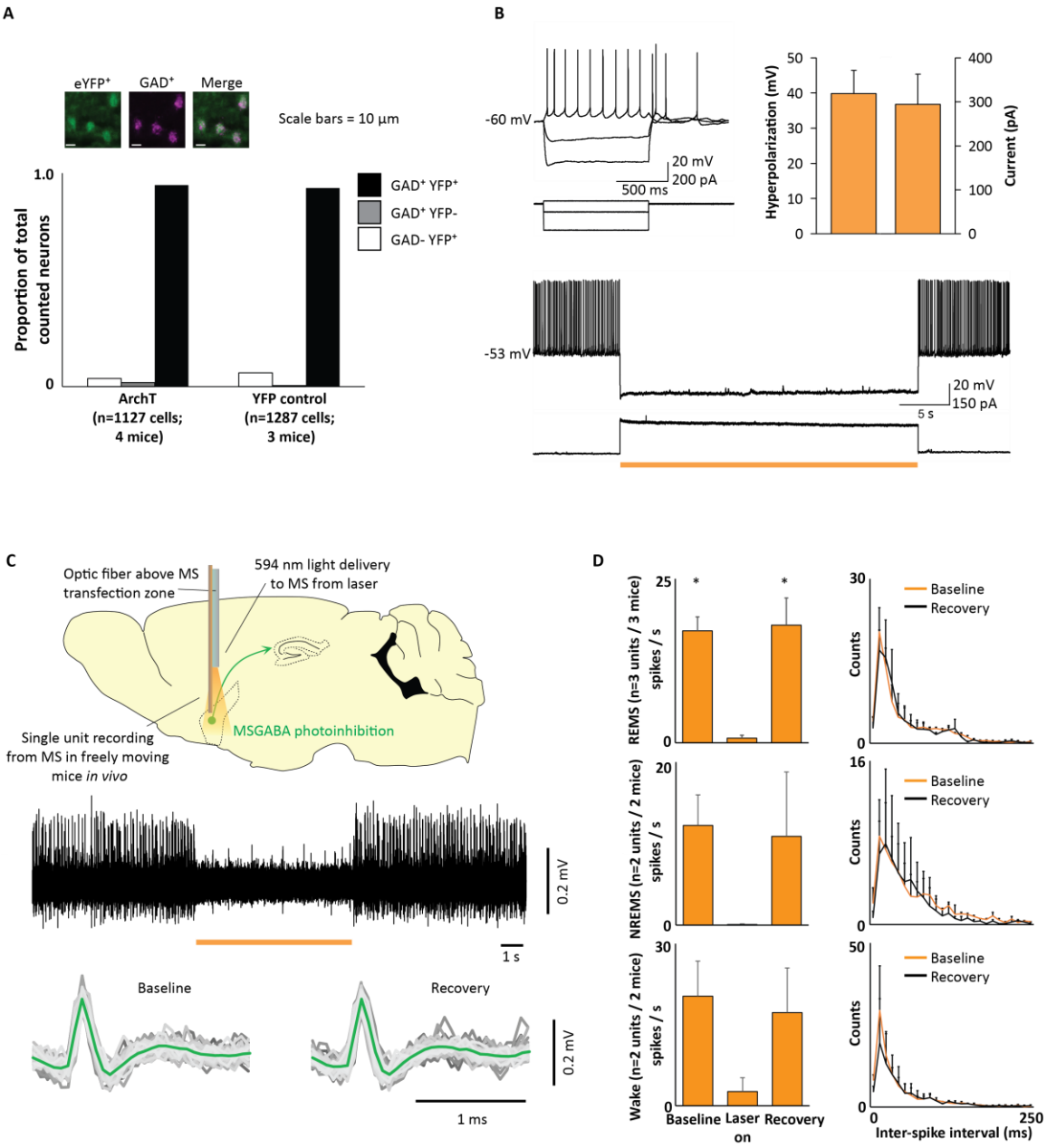
A
eYFP+
GAD+
Merge
Scale bars = 10 µm
Proportion of total counted neurons
1.0
0
GAD+ YFP+
GAD+ YFP-
GAD- YFP+
ArchT (n=1127 cells; 4 mice)
YFP control (n=1287 cells; 3 mice)
B
-60 mV
20 mV
200 pA
500 ms
Hyperpolarization (mV)
Current (pA)
-53 mV
20 mV
150 pA
5 s
C
Optic fiber above MS transfection zone
594 nm light delivery to MS from laser
MSGABA photoinhibition
Single unit recording from MS in freely moving mice in vivo
0.2 mV
1 s
Baseline
Recovery
0.2 mV
1 ms
D
REMS (n=3 units / 3 mice) spikes / s
NREMS (n=2 units / 2 mice) spikes / s
Wake (n=2 units / 2 mice) spikes / s
Baseline
Laser on
Recovery
Counts
Baseline
Recovery
Inter-spike interval (ms)

Fig. S1.
Specific targeting of ArchT-mediated inhibition to MS^{GABA} neurons. (A) Top photos show cell-specific expression of ArchT-eYFP (green) in MS^{GABA} neurons (magenta) in a VGAT::Cre mouse injected with Cre-dependent AAV. Quantified expression shown at bottom. (B) Optical inhibition of MS neurons in brain slices *in vitro*. Representative voltage traces (top, left) from an ArchT-expressing neuron responding to hyperpolarizing and depolarizing current pulses; illumination with orange light (orange bar) resulted in hyperpolarization and an outward current (bottom). Group data shown at top right. (C) Schematic (top) of *in vivo* optrode recording; an optic fiber and tetrode were placed above and within the MS, respectively, for recording transfected MS^{GABA} neurons in vivo. A filtered single unit recording during REMS showing precise inhibition of spiking during optical silencing is shown in middle. Spike waveforms for the 5 s pre-inhibition (baseline) period is shown at bottom left with average waveform overlaying in green; 5 s post-inhibition (recovery) waveform data is shown at bottom right. (D) Effect of optical inhibition on spiking rate (left) and inter-spike interval (right) of putative MS^{GABA} neurons during different states in freely behaving mice *in vivo* (n = 3 REMS, n = 2 NREMS/wake; *$P < 0.05$, Kruskal-Wallis test).

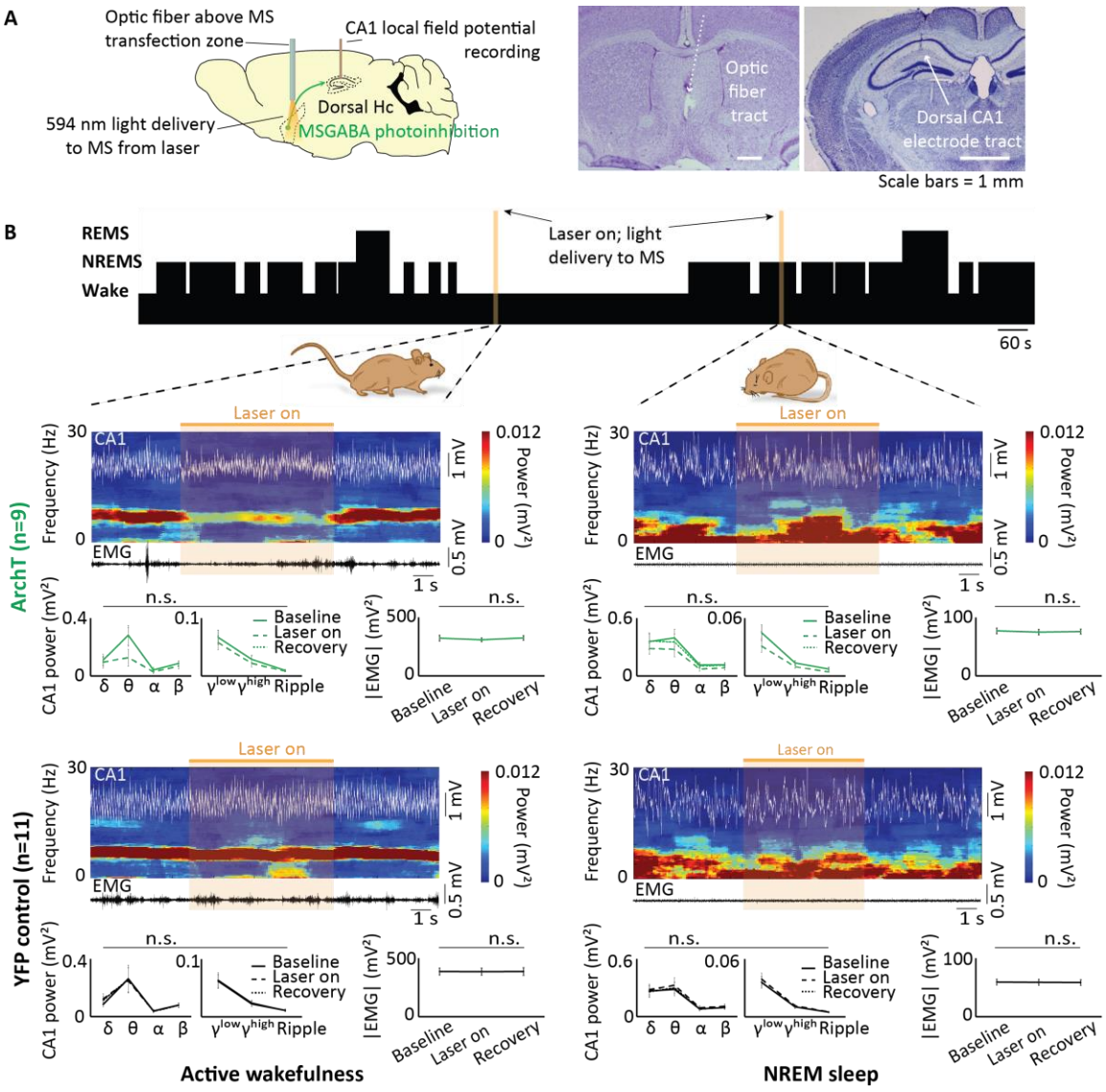
A
Optic fiber above MS transfection zone
CA1 local field potential recording
Dorsal Hc
MSGABA photoinhibition
594 nm light delivery to MS from laser
Optic fiber tract
Dorsal CA1 electrode tract
Scale bars = 1 mm
B
REMS
NREMS
Wake
Laser on; light delivery to MS
60 s
ArchT (n=9)
YFP control (n=11)
Laser on
CA1
Frequency (Hz)
Power (mV²)
EMG
1 mV
0.5 mV
1 s
CA1 power (mV²)
n.s.
Baseline
Laser on
Recovery
δ θ α β
γlow γhigh Ripple
|EMG| (mV²)
Active wakefulness
NREM sleep

Fig. S2

ArchT-mediated inhibition of MS^{GABA} neurons during NREMS and wakefulness. (A) Schematic of *in vivo* recording configuration; an optic fiber placed above the MS (histology sample in first photo at right) delivered orange laser light to the MS transfection zone allowing for optogenetic inhibition of MS^{GABA} neurons while LFP recordings were completed from electrodes implanted in dorsal CA1 (histology sample in second photo at right). An EMG inserted in the neck musculature (not depicted) simultaneously recorded muscle tone. (B) Effect of MS^{GABA} neural inhibition during active wakefulness (data on left) and NREMS (data on right) on CA1LFP and EMG activity. Mice injected with a control virus resulting in expression of only eYFP in MS^{GABA} neurons controlled for use of orange light (YFP control) (n = 9 ArchT, n = 11 YFP control; n.s. = not significant, 2-way ANOVA).

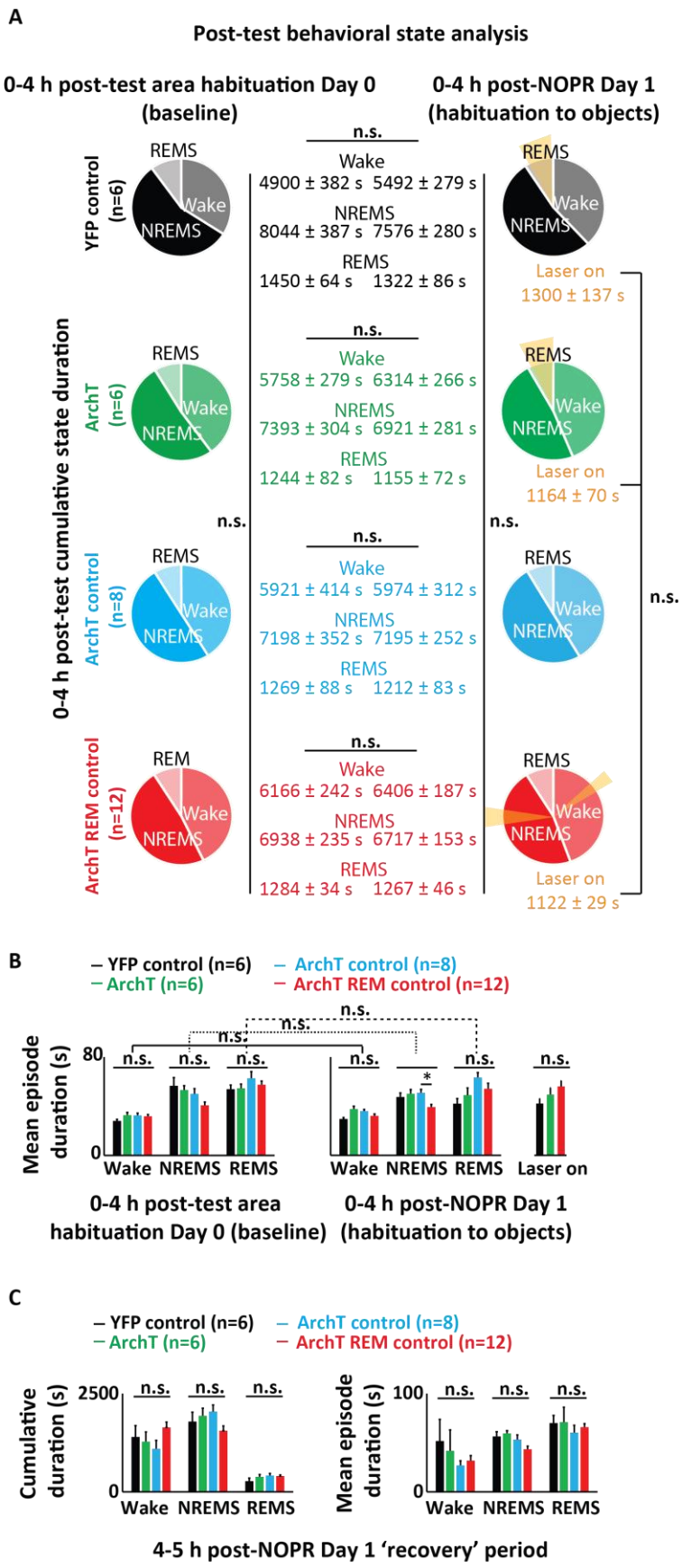
A
Post-test behavioral state analysis
0-4 h post-test area habituation Day 0 (baseline)
0-4 h post-NOPR Day 1 (habituation to objects)
0-4 h post-test cumulative state duration
YFP control (n=6)
ArchT (n=6)
ArchT control (n=8)
ArchT REM control (n=12)
REMS
REM
Wake
NREMS
n.s.
Wake
4900 ± 382 s 5492 ± 279 s
NREMS
8044 ± 387 s 7576 ± 280 s
REMS
1450 ± 64 s 1322 ± 86 s
Laser on
1300 ± 137 s
Wake
5758 ± 279 s 6314 ± 266 s
NREMS
7393 ± 304 s 6921 ± 281 s
REMS
1244 ± 82 s 1155 ± 72 s
Laser on
1164 ± 70 s
Wake
5921 ± 414 s 5974 ± 312 s
NREMS
7198 ± 352 s 7195 ± 252 s
REMS
1269 ± 88 s 1212 ± 83 s
Wake
6166 ± 242 s 6406 ± 187 s
NREMS
6938 ± 235 s 6717 ± 153 s
REMS
1284 ± 34 s 1267 ± 46 s
Laser on
1122 ± 29 s
B
YFP control (n=6)
ArchT (n=6)
ArchT control (n=8)
ArchT REM control (n=12)
Mean episode duration (s)
80
0
n.s.
*
Wake NREMS REMS
Wake NREMS REMS Laser on
0-4 h post-test area habituation Day 0 (baseline)
0-4 h post-NOPR Day 1 (habituation to objects)
C
YFP control (n=6)
ArchT (n=6)
ArchT control (n=8)
ArchT REM control (n=12)
Cumulative duration (s)
2500
0
Mean episode duration (s)
100
0
Wake NREMS REMS
4-5 h post-NOPR Day 1 'recovery' period

Fig. S3

NOPR post-test vigilance state analysis. (A,B) Comparison of vigilance state cumulative (A) and average (B) duration between groups for 4 h Day 1 (D1) post-test period and within groups vs. baseline condition (4 h period following initial habituation to NOPR test area) (n = 6 ArchT, n = 6 YFP control, n = 8 ArchT control, n = 12 ArchT REM control; *P < 0.05, n.s. = not significant, 2-way ANOVA for between group comparison; 2-way repeated-measures ANOVA for baseline vs. D1 within-group comparison). (C) Comparison of vigilance state cumulative (left) and average (right) duration between groups for 4-5 h D1 post-test 'recovery' period (4-5 h D1 post-test period when MS^{GABA} neural photoinhibition no longer occurs) (n = 6 ArchT, n = 6 YFP control, n = 8 ArchT control, n = 12 ArchT REM control; n.s. = not significant, 2-way ANOVA between group comparison).

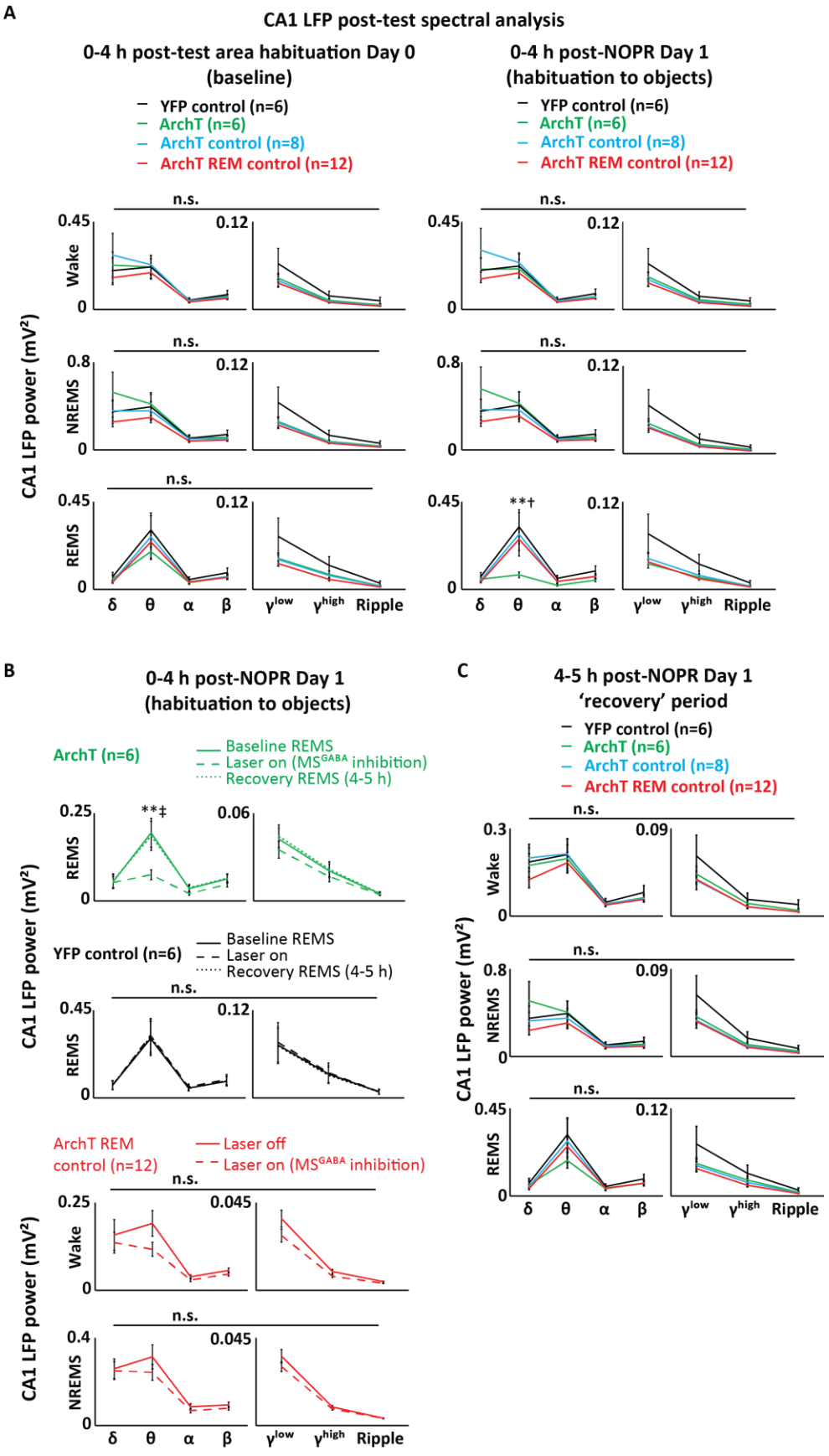
A
CA1 LFP post-test spectral analysis
0-4 h post-test area habituation Day 0 (baseline)
0-4 h post-NOPR Day 1 (habituation to objects)
YFP control (n=6)
ArchT (n=6)
ArchT control (n=8)
ArchT REM control (n=12)
CA1 LFP power (mV²)
Wake
NREMS
REMS
n.s.
**†
δ θ α β γlow γhigh Ripple
B
0-4 h post-NOPR Day 1 (habituation to objects)
ArchT (n=6)
Baseline REMS
Laser on (MSGABA inhibition)
Recovery REMS (4-5 h)
**‡
YFP control (n=6)
Laser on
ArchT REM control (n=12)
Laser off
C
4-5 h post-NOPR Day 1 'recovery' period

Fig. S4

NOPR post-test CA1LFP spectral analysis. (A) Comparison of CA1LFP spectral power for baseline condition and 4 h Day 1 (D1) post-test period (n = 6 ArchT, n = 6 YFP control, n = 8 ArchT control, n = 12 ArchT REM control; **†P < 0.01 (ArchT vs. all other groups), n.s. = not significant, 2-way ANOVA). (B) Top: Comparison of CA1LFP spectral power between baseline condition, 4 h D1 post-test period, and recovery period (4-5 h D1 post-test period when MS^{GABA} neural photoinhibition no longer occurs) (n = 6 ArchT, n = 6 YFP control; **‡P < 0.01 (REM with laser on vs. baseline and recovery REMS), n.s. = not significant, 2-way repeated-measures ANOVA). Bottom: CA1LFP spectral power in ArchT REM control mice on 4 h D1 post-test period when laser is on vs. off (n = 12; n.s. = not significant, 2-way ANOVA). (C) Between-group comparison of CA1LFP spectral power during D1 post-test recovery period (n = 6 ArchT, n = 6 YFP control, n = 8 ArchT control, n = 12 ArchT REM control; n.s. = not significant, 2-way ANOVA).

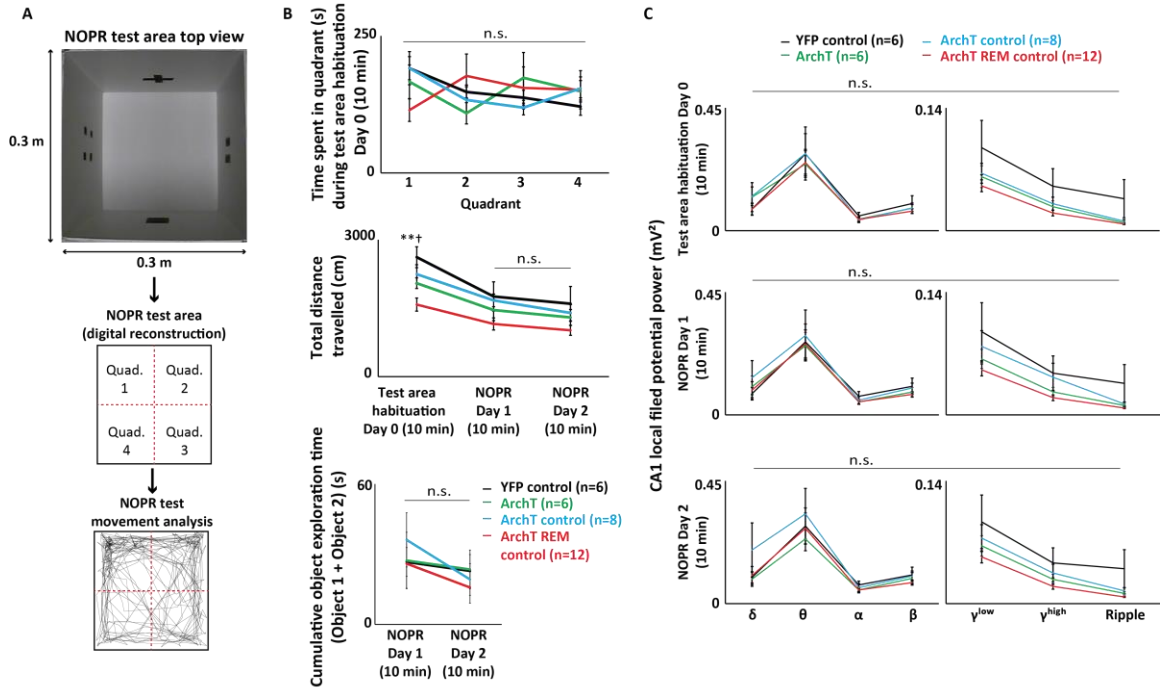
A
NOPR test area top view
0.3 m
0.3 m
NOPR test area
(digital reconstruction)
Quad. 1
Quad. 2
Quad. 4
Quad. 3
NOPR test
movement analysis
B
Time spent in quadrant (s) during test area habituation Day 0 (10 min)
250
0
n.s.
1
2
3
4
Quadrant
Total distance travelled (cm)
3000
0
**†
n.s.
Test area habituation Day 0 (10 min)
NOPR Day 1 (10 min)
NOPR Day 2 (10 min)
Cumulative object exploration time (Object 1 + Object 2) (s)
60
0
n.s.
NOPR Day 1 (10 min)
NOPR Day 2 (10 min)
YFP control (n=6)
ArchT (n=6)
ArchT control (n=8)
ArchT REM control (n=12)
C
YFP control (n=6)
ArchT (n=6)
ArchT control (n=8)
ArchT REM control (n=12)
CA1 local filed potential power (mV²)
Test area habituation Day 0 (10 min)
NOPR Day 1 (10 min)
NOPR Day 2 (10 min)
n.s.
0.45
0.14
0
δ
θ
α
β
γlow
γhigh
Ripple

Fig. S5

NOPR test movement and CA1LFP spectral analysis. (A) Schematic of NOPR movement analysis. Movement of mice during each test session (Test area habituation Day 0, Day 1 (D1), Day 2 (D2)) was quantified digitally; for preferred location analysis completed during initial test area habituation, the test area was divided into 4 quadrants digitally. (B) Movement data for NOPR test sessions. Quadrant distribution for first exposure to the NOPR test area when no objects were present (Test area habituation) is shown at top. Distance travelled during each test session is shown in middle. Cumulative object exploration time for D1 and D2 is shown at bottom. (C) Spectral analysis of CA1LFP recordings during each test session. (B-C) (n = 6 ArchT, n = 6 YFP control, n = 8 ArchT control, n = 12 ArchT REM control; **†$P < 0.01$ (YFP control vs. ArchT REM control), n.s. = not significant, 2-way repeated-measures ANOVA with Tukey post-hoc test 2-way ANOVA).

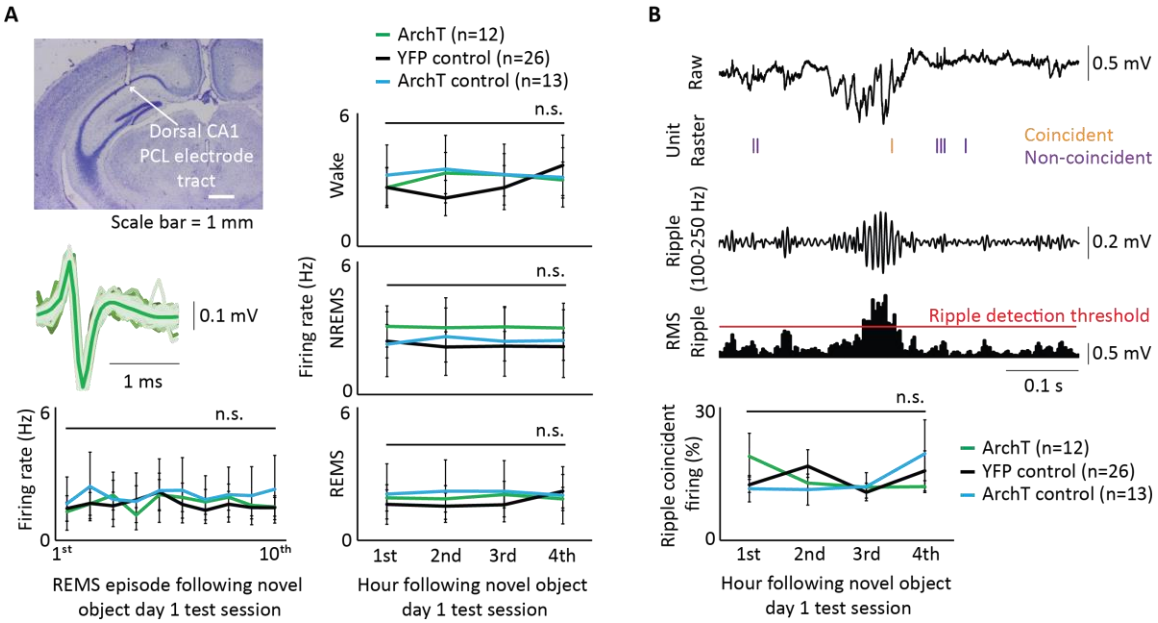
A
Dorsal CA1
PCL electrode
tract
Scale bar = 1 mm
0.1 mV
1 ms
Firing rate (Hz)
n.s.
1st
10th
REMS episode following novel
object day 1 test session
ArchT (n=12)
YFP control (n=26)
ArchT control (n=13)
Wake
NREMS
REMS
1st
2nd
3rd
4th
Hour following novel object
day 1 test session
B
Raw
0.5 mV
Unit
Raster
Coincident
Non-coincident
Ripple
(100-250 Hz)
0.2 mV
RMS
Ripple
Ripple detection threshold
0.5 mV
0.1 s
Ripple coincident
firing (%)
ArchT (n=12)
YFP control (n=26)
ArchT control (n=13)
Hour following novel object
day 1 test session

Fig. S6

CA1 physiology during 4 h REMS-selective MS^{GABA} neural silencing protocol. (A) Basic firing properties of neurons isolated from the dorsal CA1 pyramidal cell layer (PCL) (top and middle, left) were analyzed following the NOPR D1 test. Bottom, left: Unit firing frequency during REMS episodes occurring successively following testing. Right: State-specific unit rate analysis 0-4 h following testing (n = 12 units (4 mice) ArchT, n = 26 units (5 mice) YFP control, n = 13 units (5 mice) ArchT control, insufficient n ArchT REM control; n.s. = not significant, Kruskal-Wallis test). (B) Coincident unit firing probability during ripples recorded from the CA1 PCL. Top: Example of ripple detection (bottom bar graph) from ripple-filtered (middle trace) raw data (top trace). The proportion of unit timestamps occurring during detected ripples was calculated 0-4 h following NOPR D1 testing (bottom) (n = 12 units (4 mice) ArchT, n = 26 units (5 mice) YFP control, n = 13 units (5 mice) ArchT control, insufficient n ArchT REM control; n.s. = not significant, Kruskal-Wallis test).

A

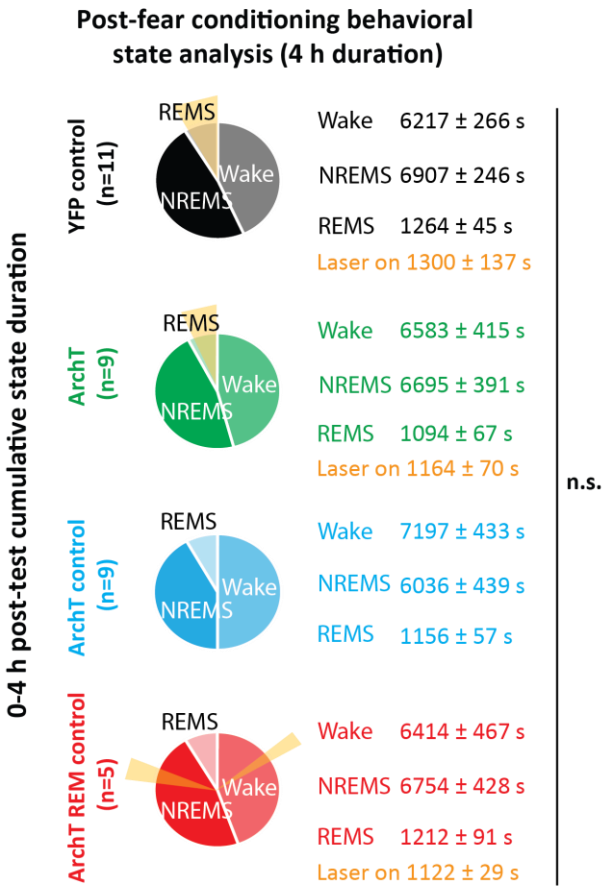
Post-fear conditioning behavioral state analysis (4 h duration)
0-4 h post-test cumulative state duration
YFP control (n=11)
REMS
Wake
NREMS
Wake 6217 ± 266 s
NREMS 6907 ± 246 s
REMS 1264 ± 45 s
Laser on 1300 ± 137 s
ArchT (n=9)
REMS
Wake
NREMS
Wake 6583 ± 415 s
NREMS 6695 ± 391 s
REMS 1094 ± 67 s
Laser on 1164 ± 70 s
ArchT control (n=9)
REMS
Wake
NREMS
Wake 7197 ± 433 s
NREMS 6036 ± 439 s
REMS 1156 ± 57 s
ArchT REM control (n=5)
REMS
Wake
NREMS
Wake 6414 ± 467 s
NREMS 6754 ± 428 s
REMS 1212 ± 91 s
Laser on 1122 ± 29 s
n.s.

B

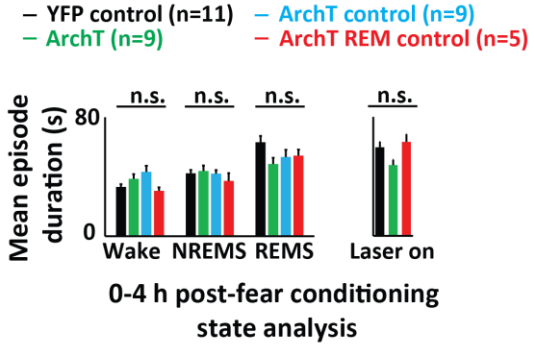
YFP control (n=11)
ArchT control (n=9)
ArchT (n=9)
ArchT REM control (n=5)
Mean episode duration (s)
80
0
n.s.
n.s.
n.s.
n.s.
Wake
NREMS
REMS
Laser on
0-4 h post-fear conditioning state analysis

C

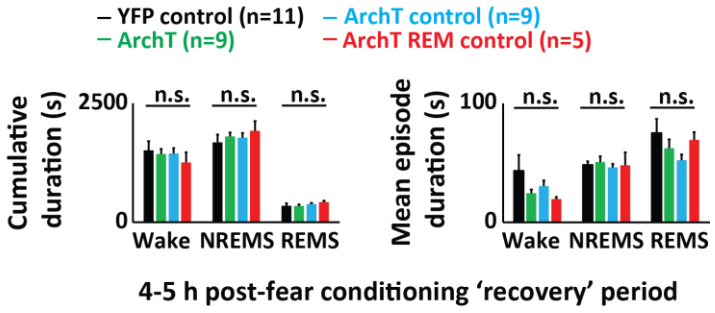
YFP control (n=11)
ArchT control (n=9)
ArchT (n=9)
ArchT REM control (n=5)
Cumulative duration (s)
2500
0
n.s.
n.s.
n.s.
Wake
NREMS
REMS
Mean episode duration (s)
100
0
n.s.
n.s.
n.s.
Wake
NREMS
REMS
4-5 h post-fear conditioning 'recovery' period

Fig. S7

Comparison of vigilance state cumulative (A) and average (B) duration between groups for 4 h Day 1 (D1) post-fear conditioning period (n = 9 ArchT, n = 11 YFP control, n = 9 ArchT control, n = 5 ArchT REM control; n.s. = not significant, 2-way ANOVA). (C) Comparison of vigilance state cumulative (left) and average (right) duration between groups for 4-5 h D1 post-fear conditioning 'recovery' period (4-5 h period when MS^{GABA} neural photoinhibition no longer occurs) (n = 9 ArchT, n = 11 YFP control, n = 9 ArchT control, n = 5 ArchT REM control; n.s. = not significant, 2-way ANOVA).

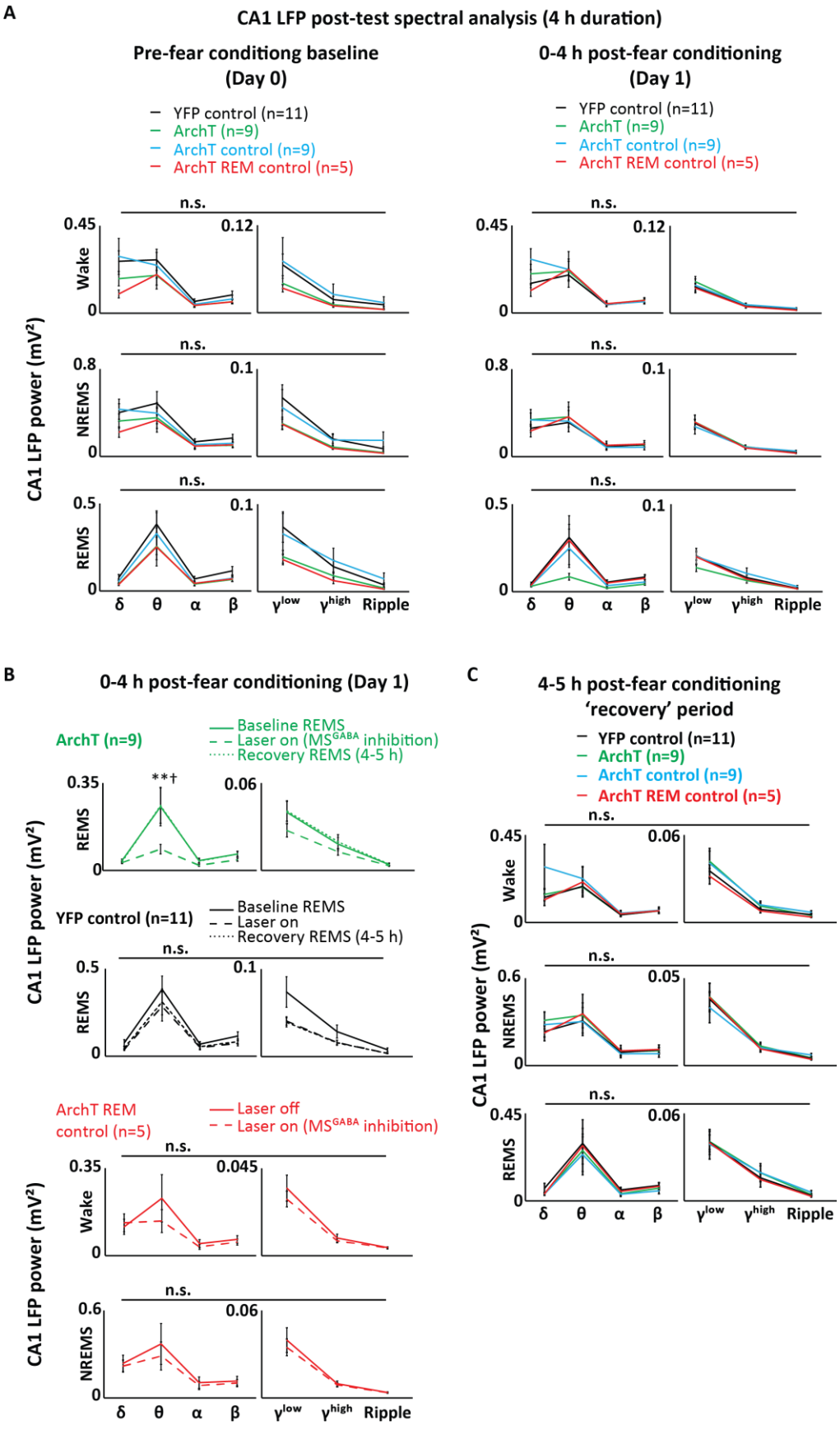
A
CA1 LFP post-test spectral analysis (4 h duration)
Pre-fear conditiong baseline (Day 0)
0-4 h post-fear conditioning (Day 1)
YFP control (n=11)
ArchT (n=9)
ArchT control (n=9)
ArchT REM control (n=5)
CA1 LFP power (mV²)
Wake
NREMS
REMS
n.s.
δ θ α β γlow γhigh Ripple
B
0-4 h post-fear conditioning (Day 1)
ArchT (n=9)
Baseline REMS
Laser on (MSGABA inhibition)
Recovery REMS (4-5 h)
**†
YFP control (n=11)
Baseline REMS
Laser on
Recovery REMS (4-5 h)
ArchT REM control (n=5)
Laser off
Laser on (MSGABA inhibition)
C
4-5 h post-fear conditioning 'recovery' period

Fig. S8

Post-fear conditioning CA1LFP spectral analysis. (A) Comparison of CA1LFP spectral power for baseline condition (4 h recording starting ~24 h prior to fear conditioning) and 4 h Day 1 (D1) post-fear conditioning period (n = 9 ArchT, n = 11 YFP control, n = 9 ArchT control, n = 5 ArchT REM control; n.s. = not significant, 2-way ANOVA). (B) Top: Comparison of CA1LFP spectral power between baseline condition, 4 h D1 post-fear conditioning period, and recovery period (4-5 h D1 post-fear conditioning period when MS^{GABA} neural photoinhibition no longer occurs) (n = 9 ArchT, n = 11 YFP control; **‡P < 0.01 (REM with laser on vs. baseline and recovery REMS), n.s. = not significant, 2-way repeated-measures ANOVA). Bottom: Comparison of CA1LFP spectral power in ArchT REM control mice on 4 h D1 post-test period when laser is on vs. off (n = 5; n.s. = not significant, 2-way ANOVA). (C) Between-group comparison of CA1 LP spectral power during D1 post-fear conditioning recovery period (n = 9 ArchT, n = 11 YFP control, n = 9 ArchT control, n = 5 ArchT REM control; n.s. = not significant, 2-way ANOVA).

Table S1.

Analysis of EEG spindle characteristics during NREMS occurring within 0-4 h NOPR Day 0 (baseline) post-test period (n = 6 ArchT, n = 6 YFP control, n = 8 ArchT control, n = 12 ArchT REM control; non-significance indicated by absence of symbols, 2-way ANOVA between groups, repeated-measures ANOVA Day 0 vs. Day 1 post-test period (Table S2) within groups).

Spindle Parameter (Window (30 s) mean)	YFP Control (n=6)	ArchT (n=6)	ArchT Control (n=8)	ArchT REM Control (n=12)
Number	2.14 ± 0.02	1.99 ± 0.03	2.06 ± 0.04	2.07 ± 0.04
Density (spindles / s)	0.071 ± 0.001	0.066 ± 0.001	0.069 ± 0.001	0.069 ± 0.001
Spindle duration (ms)	780 ± 6	761 ± 5	774 ± 5	778 ± 6
Max spindle amp (mV)	0.07 ± 0.01	0.06 ± 0.00	0.11 ± 0.04	0.09 ± 0.02
Spindle magnitude (∫)	36 ± 3	32 ± 1	58 ± 22	38 ± 10

Table S2.

Analysis of EEG spindle characteristics during NREMS occurring within 0-4 h NOPR Day 1 post-test period (n = 6 ArchT, n = 6 YFP control, n = 8 ArchT control, n = 12 ArchT REM control; non-significance indicated by absence of symbols, 2-way ANOVA between groups, repeated-measures ANOVA Day 0 (baseline (Table S1)) vs. Day 1 post-test period (Day 1) within groups).

Spindle Parameter (Window (30 s) mean)	YFP Control (n=6)	ArchT (n=6)	ArchT Control (n=8)	ArchT REM Control (n=12)
Number	2.14 ± 0.04	2.05 ± 0.04	2.02 ± 0.05	2.08 ± 0.05
Density (spindles / s)	0.072 ± 0.001	0.068 ± 0.001	0.067 ± 0.002	0.069 ± 0.001
Spindle duration (ms)	774 ± 7	783 ± 5	783 ± 12	776 ± 5
Max spindle amp (mV)	0.12 ± 0.05	0.11 ± 0.05	0.07 ± 0.01	0.07 ± 0.00
Spindle magnitude (∫)	59 ± 23	54 ± 24	38 ± 3	38 ± 2

Table S3.

Analysis of EEG spindle characteristics during NREMS occurring within 4-5 h NOPR Day 1 post-test 'recovery' period (n=6 ArchT, n=6 YFP control, n=8 ArchT control, n=12 ArchT REM control; non-significance indicated by absence of symbols, 2-way ANOVA between groups).

Spindle parameter (Window (30 s) mean)	YFP Control (n=6)	ArchT (n=6)	ArchT Control (n=8)	ArchT REM Control (n=12)
Number	2.08 ± 0.07	2.07 ± 0.06	2.13 ± 0.08	2.07 ± 0.07
Density (spindles / s)	0.069 ± 0.002	0.069 ± 0.002	0.071 ± 0.002	0.069 ± 0.002
Spindle duration (ms)	785 ± 21	786 ± 14	771 ± 13	759 ± 14
Max spindle amp (mV)	0.068 ± 0.006	0.062 ± 0.002	0.073 ± 0.005	0.075 ± 0.003
Spindle magnitude (∫)	36 ± 7	32 ± 1	37 ± 3	38 ± 2

Table S4.

Analysis of EEG spindle characteristics during NREMS occurring within 0-4 h fear conditioning post-test period (n = 9 ArchT, n = 11 YFP control, n = 9 ArchT control, n = 5 ArchT REM control; non-significance indicated by absence of symbols, 2-way ANOVA between groups.

Spindle Parameter (Window (30 s) mean)	YFP Control (n=11)	ArchT (n=9)	ArchT Control (n=9)	ArchT REM Control (n=5)
Number	2.12 ± 0.03	2.02 ± 0.03	1.99 ± 0.04	2.08 ± 0.07
Density (spindles / s)	0.071 ± 0.001	0.067 ± 0.001	0.066 ± 0.001	0.069 ± 0.002
Spindle duration (ms)	783 ± 7	775 ± 8	793 ± 15	788 ± 9
Max spindle amp (mV)	0.076 ± 0.006	0.070 ± 0.002	0.067 ± 0.005	0.079 ± 0.008
Spindle magnitude (∫)	39 ± 3	36 ± 1	35 ± 3	40 ± 5

Table S5.

Analysis of EEG spindle characteristics during NREMS occurring within 4-5 h fear conditioning post-test 'recovery' period (n=9 ArchT, n=11 YFP control, n=9 ArchT control, n=5 ArchT REM control; non-significance indicated by absence of symbols, 2-way ANOVA between groups).

Spindle parameter (Window (30 s) mean)	YFP Control (n=11)	ArchT (n=9)	ArchT Control (n=9)	ArchT REM Control (n=5)
Number	2.17 ± 0.08	2.11 ± 0.06	1.93 ± 0.07	2.01 ± 0.07
Density (spindles / s)	0.072 ± 0.003	0.070 ± 0.002	0.064 ± 0.002	0.067 ± 0.002
Spindle duration (ms)	773 ± 13	783 ± 13	771 ± 15	794 ± 23
Max spindle amp (mV)	0.075 ± 0.007	0.069 ± 0.002	0.069 ± 0.004	0.083 ± 0.016
Spindle magnitude (∫)	39 ± 4	35 ± 1	35 ± 3	44 ± 10

Table S6.

Analysis of CA1 cell layer LFP ripple characteristics during NREMS occurring within 0-1 h NOPR Day 1 post-test period. Only data from mice that contributed to CA1 unit analysis is included (n = 4 ArchT, n = 5 YFP control, n = 4 ArchT control; non-significance indicated by absence of symbols, 2-way ANOVA between groups).

Ripple Parameter (Window (30 s) mean)	YFP Control (n=5)	ArchT (n=4)	ArchT Control (n=4)
Number	32.3 ± 1.1	31.5 ± 1.5	32.2 ± 0.4
Density (Ripples / s)	1.08 ± 0.04	1.05 ± 0.05	1.07 ± 0.01
Ripple duration (ms)	23.1 ± 1.0	23.3 ± 1.2	21.0 ± 1.8
Max ripple amp (mV)	0.18 ± 0.03	0.20 ± 0.06	0.14 ± 0.07
Ripple magnitude (∫)	3.8 ± 0.6	4.2 ± 1.5	2.9 ± 1.4

Table S7.

Analysis of CA1 cell layer LFP ripple characteristics during NREMS occurring within 1-2 h NOPR Day 1 post-test period. Only data from mice that contributed to CA1 unit analysis is included (n = 4 ArchT, n = 5 YFP control, n = 4 ArchT control; non-significance indicated by absence of symbols, 2-way ANOVA between groups).

Ripple Parameter (Window (30 s) mean)	YFP Control (n=5)	ArchT (n=4)	ArchT Control (n=4)
Number	32.0 ± 0.9	31.4 ± 0.8	33.5 ± 1.4
Density (Ripples / s)	1.07 ± 0.03	1.05 ± 0.03	0.84 ± 0.28
Ripple duration (ms)	23.1 ± 1.0	22.8 ± 1.1	21.2 ± 1.5
Max ripple amp (mV)	0.17 ± 0.03	0.19 ± 0.07	0.16 ± 0.08
Ripple magnitude (∫)	3.6 ± 0.5	4.0 ± 1.5	3.2 ± 1.6

Table S8.

Analysis of CA1 cell layer LFP ripple characteristics during NREMS occurring within 2-3 h NOPR Day 1 post-test period. Only data from mice that contributed to CA1 unit analysis is included (n = 4 ArchT, n = 5 YFP control, n = 4 ArchT control; non-significance indicated by absence of symbols, 2-way ANOVA between groups).

Ripple Parameter (Window (30 s) mean)	YFP Control (n=5)	ArchT (n=4)	ArchT Control (n=4)
Number	32.6 ± 1.5	30.7 ± 0.6	32.6 ± 1.0
Density (Ripples / s)	1.09 ± 0.05	1.02 ± 0.02	1.09 ± 0.03
Ripple duration (ms)	22.8 ± 1.0	22.5 ± 0.9	20.4 ± 1.6
Max ripple amp (mV)	0.17 ± 0.03	0.19 ± 0.06	0.14 ± 0.07
Ripple magnitude (∫)	3.5 ± 0.5	3.8 ± 1.5	2.7 ± 1.3

Table S9.

Analysis of CA1 cell layer LFP ripple characteristics during NREMS occurring within 3-4 h NOPR Day 1 post-test period. Only data from mice that contributed to CA1 unit analysis is included (n = 4 ArchT, n = 5 YFP control, n = 4 ArchT control; non-significance indicated by absence of symbols, 2-way ANOVA between groups).

Ripple Parameter (Window (30 s) mean)	YFP Control (n=5)	ArchT (n=4)	ArchT Control (n=4)
Number	30.7 ± 1.2	30.3 ± 0.9	32.0 ± 0.6
Density (Ripples / s)	1.02 ± 0.04	1.01 ± 0.03	1.07 ± 0.02
Ripple duration (ms)	23.4 ± 1.0	23.0 ± 1.1	21.1 ± 1.6
Max ripple amp (mV)	0.17 ± 0.03	0.19 ± 0.06	0.14 ± 0.06
Ripple magnitude (∫)	3.6 ± 0.6	3.9 ± 1.5	2.7 ± 1.4

REFERENCES

1. J. M. Siegel, Clues to the functions of mammalian sleep. *Nature* **437**, 1264–1271 (2005). Medline doi:10.1038/nature04285

2. S. Diekelmann, J. Born, *Sleep* **11**, 114–126 (2010).

3. R. Stickgold, M. P. Walker, Sleep and memory: The ongoing debate. *Sleep* **28**, 1225–1227 (2005). Medline

4. J. M. Siegel, The REM sleep-memory consolidation hypothesis. *Science* **294**, 1058–1063 (2001). Medline doi:10.1126/science.1063049

5. R. P. Vertes, Memory consolidation in sleep; dream or reality. *Neuron* **44**, 135–148 (2004). Medline doi:10.1016/j.neuron.2004.08.034

6. T. E. Robinson, R. C. Kramis, C. H. Vanderwolf, Two types of cerebral activation during active sleep: Relations to behavior. *Brain Res.* **124**, 544–549 (1977). Medline doi:10.1016/0006-8993(77)90954-4

7. G. Buzsáki, Theta oscillations in the hippocampus. *Neuron* **33**, 325–340 (2002). Medline doi:10.1016/S0896-6273(02)00586-X

8. G. R. Poe, D. A. Nitz, B. L. McNaughton, C. A. Barnes, Experience-dependent phase-reversal of hippocampal neuron firing during REM sleep. *Brain Res.* **855**, 176–180 (2000). Medline doi:10.1016/S0006-8993(99)02310-0

9. K. Louie, M. A. Wilson, Temporally structured replay of awake hippocampal ensemble activity during rapid eye movement sleep. *Neuron* **29**, 145–156 (2001). Medline doi:10.1016/S0896-6273(01)00186-6

10. J. D. Green, A. A. Arduini, Hippocampal electrical activity in arousal. *J. Neurophysiol.* **17**, 533–557 (1954). Medline

11. S. J. Mitchell, J. N. Rawlins, O. Steward, D. S. Olton, Medial septal area lesions disrupt theta rhythm and cholinergic staining in medial entorhinal cortex and produce impaired radial arm maze behavior in rats. *J. Neurosci.* **2**, 292–302 (1982). Medline

12. B. E. Jones, Paradoxical sleep and its chemical/structural substrates in the brain. *Neuroscience* **40**, 637–656 (1991). Medline doi:10.1016/0306-4522(91)90002-6

13. R. E. Brown, R. Basheer, J. T. McKenna, R. E. Strecker, R. W. McCarley, Control of sleep and wakefulness. *Physiol. Rev.* **92**, 1087–1187 (2012). Medline doi:10.1152/physrev.00032.2011

14. H. Petsche, C. Stumpf, G. Gogolak, The significance of the rabbit's septum as a relay station between the midbrain and the hippocampus. I. The control of hippocampus arousal activity by the septum cells. *Electroencephalogr. Clin. Neurophysiol.* **14**, 202–211 (1962). Medline doi:10.1016/0013-4694(62)90030-5

15. A. P. Simon, F. Poindessous-Jazat, P. Dutar, J. Epelbaum, M. H. Bassant, Firing properties of anatomically identified neurons in the medial septum of anesthetized and unanesthetized restrained rats. *J. Neurosci.* **26**, 9038–9046 (2006). Medline doi:10.1523/JNEUROSCI.1401-06.2006

16. K. Tóth, T. F. Freund, R. Miles, Disinhibition of rat hippocampal pyramidal cells by GABAergic afferents from the septum. *J. Physiol.* **500**, 463–474 (1997). Medline doi:10.1113/jphysiol.1997.sp022033

17. M. Antunes, G. Biala, The novel object recognition memory: Neurobiology, test procedure, and its modifications. *Cogn. Process.* **13**, 93–110 (2012). Medline doi:10.1007/s10339-011-0430-z

18. M. B. Moser, D. C. Rowland, E. I. Moser, *Cold Spring Harbor Perspect. Biol.* **7**, 1–15 (2016).

19. J. J. Kim, M. S. Fanselow, Modality-specific retrograde amnesia of fear. *Science* **256**, 675–677 (1992). Medline doi:10.1126/science.1585183

20. A. A. Borbély, A two process model of sleep regulation. *Hum. Neurobiol.* **1**, 195–204 (1982). Medline

21. A. D. Grosmark, K. Mizuseki, E. Pastalkova, K. Diba, G. Buzsáki, REM sleep reorganizes hippocampal excitability. *Neuron* **75**, 1001–1007 (2012). Medline doi:10.1016/j.neuron.2012.08.015

22. R. C. Meibach, A. Siegel, Efferent connections of the septal area in the rat: An analysis utilizing retrograde and anterograde transport methods. *Brain Res.* **119**, 1–20 (1977). Medline doi:10.1016/0006-8993(77)90088-9

23. M. E. Hasselmo, Temporally structured replay of neural activity in a model of entorhinal cortex, hippocampus and postsubiculum. *Eur. J. Neurosci.* **28**, 1301–1315 (2008). Medline doi:10.1111/j.1460-9568.2008.06437.x

24. P. Curzon, N. R. Rustay, K. E. Browman, in *Methods of Behavior Analysis in Neuroscience*, J. J. Buccafusco, Ed. (CRC Press, Boca Raton, FL, 2009), chap. 2.

25. R. J. Blanchard, D. C. Blanchard, Crouching as an index of fear. *Comp. Physiol. Psychol.* **67**, 370–375 (1969). doi:10.1037/h0026779

26. J. Csicsvari, H. Hirase, A. Czurko, G. Buzsáki, Reliability and state dependence of pyramidal cell-interneuron synapses in the hippocampus: An ensemble approach in the behaving rat. *Neuron* **21**, 179–189 (1998). Medline doi:10.1016/S0896-6273(00)80525-5

27. J. A. Freeman, C. Nicholson, Experimental optimization of current source-density technique for anuran cerebellum. *J. Neurophysiol.* **38**, 369–382 (1975). Medline